

Analyzing URA Geometry for Enhanced Near-Field Beamfocusing and Spatial Degrees of Freedom

Ahmed Hussain, Asmaa Abdallah *Senior Member, IEEE*, Abdulkadir Celik, *Senior Member, IEEE*, Emil Björnson, *Fellow, IEEE* and Ahmed M. Eltawil, *Senior Member, IEEE*

Abstract—With the deployment of large antenna arrays at high-frequency bands, future wireless communication systems are likely to operate in the radiative near-field. Unlike far-field beam steering, near-field beams can be focused on a spatial region with a finite depth, enabling spatial multiplexing in the range dimension. Moreover, in the line-of-sight MIMO near-field, multiple spatial degrees of freedom (DoF) are accessible, akin to a scattering-rich environment. In this paper, we derive the beamdepth for a generalized uniform rectangular array (URA) and investigate how the array geometry influences near-field beamdepth and its limits. We define the effective beamfocusing Rayleigh distance (EBRD), to present a near-field boundary with respect to beamfocusing and spatial multiplexing gains for the generalized URA. Our results demonstrate that under a fixed element count constraint, the array geometry has a strong impact on beamdepth, whereas this effect diminishes under a fixed aperture length constraint. Moreover, compared to uniform square arrays, elongated configurations such as uniform linear arrays (ULAs) yield narrower beamdepth and extend the effective near-field region defined by the EBRD. Building on these insights, we design a polar codebook for compressed-sensing-based channel estimation that leverages our findings. Simulation results show that the proposed polar codebook achieves a 2 dB NMSE improvement over state-of-the-art methods. Additionally, we present an analytical expression to quantify the effective spatial DoF in the near-field, revealing that they are also constrained by the EBRD. Notably, the maximum spatial DoF is achieved with a ULA configuration, outperforming a square URA in this regard.

Index Terms—Radiative near-field, beamdepth, codebook, spatial degree of freedom, rectangular arrays, effective beamfocusing Rayleigh distance.

I. INTRODUCTION

MASSIVE multiple-input multiple-output (MIMO) technology is a cornerstone of fifth generation (5G) system advancements. Building on this foundation, future wireless networks are anticipated to leverage even larger antenna arrays, such as ultra-massive (UM)-MIMO, while progressing toward higher frequency spectra [2]. As carrier frequencies increase, the corresponding wavelengths decrease, enabling the deployment of larger antenna arrays within the given array size. The electromagnetic phenomenon surrounding an antenna array is typically divided into three regions: the reactive near-field, the radiative near-field, and the far-field. In this work, we

refer to the radiative near-field simply as the near-field, which extends from the edge of the reactive zone out to the Rayleigh distance. Within this region, energy propagates with spherical wavefronts and exhibits distance-dependent characteristics. Beyond the Rayleigh distance—which marks the boundary between the radiative near-field and the far-field—the curvature of wavefronts diminishes, allowing them to be approximated as planar waves with a phase error of less than $\pi/8$ [3].

Qualcomm recently unveiled a 4096-element Giga-MIMO prototype operating at 13 GHz, integrated within a form factor comparable to existing 256-element 5G base stations (BSs) [4]. This advancement exemplifies a broader trend in future wireless systems: scaling up antenna arrays either by increasing the number of elements—enabled by higher carrier frequencies—or by expanding the physical aperture. Both approaches inherently enlarge the radiative near-field region, making it a significant portion of the communication region. Contemporary research underscores the potential of near-field propagation to enhance both single-user and multiuser communication capacity [5]. In the near-field regime, the finite beamdepth enables spatial separation of users located within the same angular direction, thereby improving multiuser capacity [6] for randomly located users. Simultaneously, the curvature of spherical wavefronts facilitates the transmission of multiple spatial data layers even under line-of-sight (LoS) conditions to a single multi-antenna device, thus augmenting single-user capacity [7]. Given the distance-dependent characteristics of near-field propagation, this work aims to address three fundamental research questions. First, what are the spatial boundaries—specifically, the range limits across different angles—within which near-field beamfocusing and multiple degrees of freedom (DoF) can be effectively achieved? Outside these limits, the LoS channel exhibits far-field behavior, characterized by infinite beamdepth and a single spatial DoF. Second, how does the geometry of the antenna array influence beamdepth and the extent of the near-field region, under practical constraints such as a fixed aperture size or a fixed number of antenna elements? Third, how do beam pattern characteristics in the range dimension compare to those in the angular dimension? By investigating these questions, this study seeks to derive new insights into how near-field effects can be leveraged to enhance spatial multiplexing, ultimately enabling high-capacity wireless communication systems.

Furthermore, harnessing near-field gains necessitates precise channel estimation, a challenge that becomes increasingly complex in UM-MIMO systems employing hybrid beamforming (HBF) [3]. While HBF significantly reduces hardware costs and complexity by limiting the number of radio frequency (RF)

Ahmed Hussain, Asmaa Abdallah, Abdulkadir Celik, and Ahmed M. Eltawil are with Computer, Electrical, and Mathematical Sciences and Engineering (CEMSE) Division, King Abdullah University of Science and Technology (KAUST), Thuwal, 23955-6900, KSA. Emil Björnson is with the School of Electrical Engineering and Computer Science, KTH Royal Institute of Technology, 100 44 Stockholm, Sweden. The work of E. Björnson was supported by the Grant 2022-04222 from the Swedish Research Council. A conference version of this work is accepted in IEEE PIMRC 2025 [1].

chains, it also constrains the number of observable in-phase and quadrature-phase (IQ) samples. As a result, achieving reliable channel estimates demands a higher pilot overhead, highlighting the need for efficient estimation techniques along with polar codebook designs specifically tailored to near-field conditions. While polar codebooks for uniform linear arrays (ULAs) have been studied in [8], [9], practical systems predominantly employ uniform rectangular arrays (URAs), which accommodate a larger number of antenna elements within a constrained physical area. The polar codebooks developed for ULAs are not directly applicable to URAs due to their complex array gain functions. Moreover, the analysis and design of URA-based polar codebooks is challenging because of the coupling among azimuth, elevation, and range parameters.

A. Related Work

Foundational work on near-field beamforming [10] derived beamdepth expressions for square aperture antennas, later extended to planar arrays in [11]. Notably, the beamdepth analyses in [10], [11] are based on continuous aperture (CAP) antennas, where the Rayleigh distance of the array is defined as the product of the number of antenna elements and the Rayleigh distance of the individual antenna element. In contrast, we define the Rayleigh distance of the array as $r_{\text{RD}} = \frac{2D^2}{\lambda}$, where D represents the aperture length of the antenna array. Furthermore, explicit closed-form beamdepth expressions in [10], [11] are limited to boresight transmissions, underscoring the need for angle-dependent beamdepth analysis for spatially discrete (SPD) antennas.

The capacity of a MIMO system grows linearly with the spatial DoF, which are influenced by both the scattering environment and the array geometry [12]. For large CAP antennas, the spatial DoF are fundamentally bounded by $\frac{2}{\lambda}$ per meter for a linear segment and $\frac{\pi}{\lambda^2}$ per square meter for planar segments [13]. The maximum spatial DoF is limited by the number of antenna elements and is the same in both near and far-field [7]. Maximum spatial DoF in the LoS far-field channel equals one; however, spherical wavefronts in the near-field enable access to enhanced spatial DoF. Given a constraint on a fixed number of antenna elements, we aim to determine the angle-dependent limit within the near-field where the spatial DoF exceeds one for different array geometries.

Recent studies have indicated that the classical Rayleigh distance often overestimates the extent of the effective near-field region [14], prompting the development of alternative metrics to more accurately characterize near-field effects and predict when they can be utilized to achieve more well-conditioned channels. To model a wideband near-field channel, [15] introduced the concept of effective Rayleigh distance (ERD), based on far-field beamforming loss in the near-field region, and this idea was expanded to wideband phased arrays with the bandwidth-aware near-field distance (BAND) [16]. The ERD and the BAND cover only a small fraction of the near-field region, as defined by the Rayleigh distance. However, these metrics are based on far-field beamforming loss and therefore do not adequately capture near-field effects. The effective beamfocusing Rayleigh distance (EBRD) metric was proposed

in [8] to characterize the limits of polar-domain sparsity for ULAs. Despite these advancements, an angle-dependent spatial limit for URAs—one that jointly characterizes beamfocusing and spatial DoF—remains undetermined.

Near-field beamfocusing requires geometry-dependent phase compensation to account for spherical wavefront curvature. In particular, the achievable beamdepth is governed by the effective aperture length, which is determined by the diagonal (i.e., the maximum dimension) of the URA. In this context, further research is needed to investigate array geometries that enable narrow beamdepth and extended near-field boundaries, to guide the design of future networks that enable more users to benefit from near-field propagation. This paper addresses these gaps by exploring the interplay of array geometry and near-field electromagnetic properties. Herein, we present a comprehensive analysis of the near-field beam pattern, examining key metrics such as beamdepth, limits of the beamdepth, beam resolution, spatial DoF, and the influence of array geometry on these parameters. In contrast to [11], we derive angle-dependent expressions for near-field beamfocusing. Moreover, we exploit this characterization to design polar codebooks for near-field channel estimation.

B. Contribution

This work explores near-field beamfocusing for an SPD URA with a generic width-to-height ratio. We derive the normalized array gain using Fresnel functions, based on which we formulate a beamdepth expression. Additionally, we establish angle-dependent limits for beamfocusing and characterize the near-field beam pattern in terms of resolution and sidelobe levels across both the range and angular dimensions. Furthermore, we examine the influence of spatial focus regions and array geometry on near-field beamdepth. Drawing inspiration from the far-field codebook in the angular domain—where beams spaced by the 3 dB angular beamwidth have minimum correlation while maximizing the coverage—we propose constructing a polar codebook where codewords are separated by the beamdepth in the distance dimension. We also characterize the near-field spatial DoF using a Fresnel-based gain function and investigate how the array geometry affects these spatial DoF. The main contributions of this paper are summarized below:

- **Beamdepth and effective beamfocusing Rayleigh distance:** We derive a closed-form beamdepth and EBRD expression for a URA, establishing the maximum angle-dependent range limit for finite-depth beams. Our analysis demonstrates how array geometry influences both beamdepth and EBRD, providing critical insights for enhancing multiuser capacity in near-field communication.
- **Characterization of near-field beam pattern:** We compare and contrast near-field beam patterns across range and angle dimensions with respect to beam resolution and sidelobe levels. Furthermore, we propose a window function that attenuates sidelobes in the range dimension.
- **Spatial degrees of freedom:** We derive a Fresnel-based gain function to characterize the effective degrees of freedom (EDoF) across different array geometries.

Furthermore, we analyze the boundary beyond which the EDoF in the near-field and far-field become equivalent.

- **Polar codebook design:** Leveraging the near-field beamforming and beam pattern analysis, we propose a novel polar codebook tailored for near-field channel estimation in a URA. The proposed codebook enhances channel estimation performance by constructing codewords with low column coherence while improving computational efficiency through a reduced codebook size.

C. Notations and Organization of the Paper

Matrices, vectors, and scalars are denoted by bold uppercase, bold lowercase, and lowercase letters, respectively. The expectation, transpose, and conjugate transpose operations are denoted by $\mathbb{E}[\cdot]$, $(\cdot)^T$, and $(\cdot)^H$ respectively. The uniform distribution between a and b is annotated by $\mathcal{U}(a, b)$. Furthermore, \odot represents the Hadamard product.

The remainder of the paper is structured as follows. Section II presents the near-field channel model, followed by Section III, which derives the beamdepth and the EBRD. Section IV analyzes the near-field beam pattern, and Section V characterizes the spatial DoF. The design of the polar codebook is detailed in Section VI, and conclusions are drawn in Section VII.

II. SYSTEM MODEL

We consider a narrow-band communication system equipped with a UM scale antenna array at the BS and a single isotropic antenna user equipment (UE) as depicted in Fig. 1. The antenna array consists of a URA with N_{BS} small antennas, arranged with N_1 elements along the y-axis and N_2 elements along the z-axis, respectively. The element spacing along both axes is the same and equals $d_y = d_z = d = \frac{\lambda}{2}$. Antenna elements along the y-axis are indexed as $n_1 \in [-\tilde{N}_1, \dots, 0, \dots, \tilde{N}_1 - 1]$ where $\tilde{N}_1 = \frac{N_1}{2}$. Likewise, the antenna elements along z-axis are indexed as $n_2 \in [-\tilde{N}_2, \dots, 0, \dots, \tilde{N}_2 - 1]$ where $\tilde{N}_2 = \frac{N_2}{2}$. The aperture length of the URA can be determined from the Pythagorean theorem as $D = d\sqrt{N_1^2 + N_2^2}$. The aspect ratio of the array is defined as $\eta = \frac{N_1}{N_2}$. When $\eta > 1$, the array exhibits a wide configuration, whereas $\eta < 1$ corresponds to a tall configuration. In the extreme cases where $\eta \gg 1$ or $\eta \ll 1$, the URA approaches a ULA. In particular, a ULA is obtained when its physical length equals the aperture length D . The UE subtends azimuth angle φ , elevation angle θ , and is positioned at a distance r from the BS. In this paper, the minimum distance in the radiative near-field is set as $2D$ such that amplitude variations across the array are negligible, and accordingly, a uniform spherical wave (USW) model is employed [17]. The normalized near-field array response vector for a ULA with N_1 antenna elements is expressed as

$$\mathbf{b}_{\text{ULA}}(\varphi, r) = \frac{1}{\sqrt{N_1}} \left[e^{-j\nu(r(-\tilde{N}_1)-r)}, \dots, e^{-j\nu(r(\tilde{N}_1)-r)} \right], \quad (1)$$

where $\nu = \frac{2\pi f_c}{c}$ is the wavenumber, with f_c as the carrier frequency and $r^{(n)}$ is the distance between the UE and the n^{th} antenna element of the ULA. For a URA with $N_{\text{BS}} = N_1 N_2$

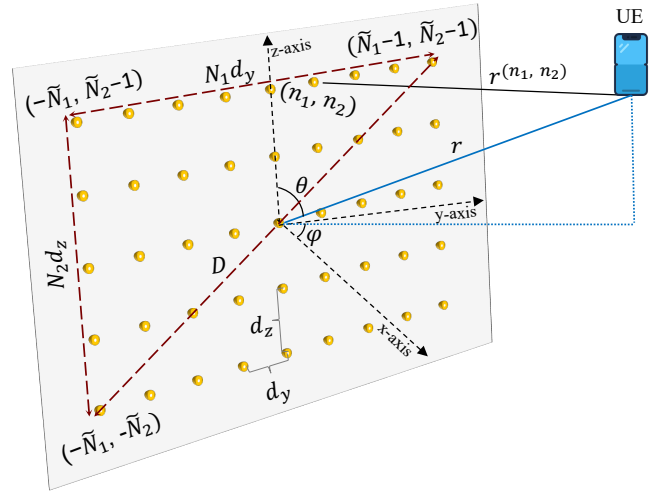


Fig. 1: URA setup and a single prospective user.

elements, the near-field array response vector $\mathbf{b}_{\text{URA}}(\varphi, \theta, r)$ can be obtained based on the spherical-wave propagation model as

$$\mathbf{b}_{\text{URA}}(\varphi, \theta, r) = \frac{1}{\sqrt{N_{\text{BS}}}} \left[e^{-j\nu(r^{(-\tilde{\zeta})}-r)}, \dots, e^{-j\nu(r^{(\tilde{\zeta})}-r)} \right], \quad (2)$$

where $\tilde{\zeta} = (\tilde{N}_1, \tilde{N}_2)$. The distance $r^{(n_1, n_2)}$ between the UE and $(n_1, n_2)^{\text{th}}$ element of the URA is given by

$$\begin{aligned} r^{(n_1, n_2)} &= \sqrt{(ru_x - 0)^2 + (ru_y - n_1 d)^2 + (ru_z - n_2 d)^2}, \\ &\stackrel{(a)}{\approx} r - n_1 d u_y - n_2 d u_z + \frac{n_1^2 d^2}{2r} \beta_1 \dots \\ &\quad + \frac{n_2^2 d^2}{2r} \beta_2 - \frac{n_1 n_2 d^2 u_y u_z}{r}, \\ &\stackrel{(b)}{\approx} r - n_1 d u_y - n_2 d u_z + \frac{n_1^2 d^2}{2r} \beta_1 + \frac{n_2^2 d^2}{2r} \beta_2, \end{aligned} \quad (3)$$

where the directional cosines are $u_x = \sin \theta \cos \varphi$, $u_y = \sin \theta \sin \varphi$, and $u_z = \cos \theta$. Approximation (a), also termed the *near-field expansion*, is derived from the second-order Taylor expansion $\sqrt{1+x} \approx 1 + \frac{x}{2} - \frac{1}{8}x^2$, that is tight for small values of x . Furthermore, $\beta_1 = 1 - \sin^2 \theta \sin^2 \varphi$ and, $\beta_2 = 1 - \cos^2 \theta$. To make the following analysis tractable, we omit the last term in (3)(a) to obtain (3)(b), as it is negligible for large values of N_{BS} [18], and accounts for only 5% of the array gain [5]. Furthermore, when r is greater than the Rayleigh distance $r_{\text{RD}} = \frac{2D^2}{\lambda}$, the terms involving $\frac{1}{r}$ can be ignored, and (2) degenerates to the far-field steering vector

$$\begin{aligned} \mathbf{a}_{\text{URA}}(\varphi, \theta) &= \frac{1}{\sqrt{N_{\text{BS}}}} \left[e^{-j\nu d(-\tilde{N}_1 \sin \varphi \sin \theta - \tilde{N}_2 \cos \theta)}, \dots, 1, \right. \\ &\quad \left. \dots, e^{-j\nu d(\tilde{N}_1 \sin \varphi \sin \theta + \tilde{N}_2 \cos \theta)} \right] \in \mathbb{C}^{N_1 N_2 \times 1}. \end{aligned} \quad (4)$$

III. ANALYSIS OF NEAR-FIELD BEAMFORMING

Finite-depth beamforming is achievable in the radiative near-field through the conjugate phase method. In this approach, the phase of each antenna element is adjusted to compensate for the path-length difference between the focal point and the antenna element, thereby ensuring constructive interference at the focal point. The resulting beam, as depicted in Fig.

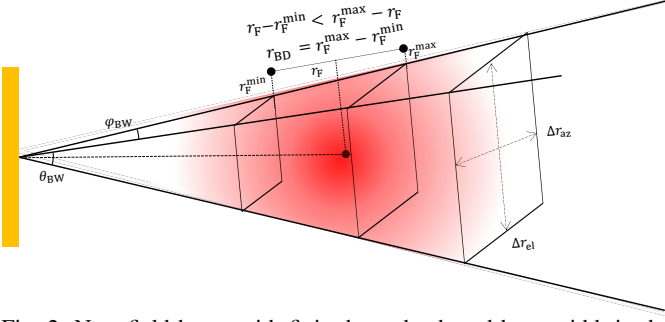


Fig. 2: Near-field beam with finite beamdepth and beamwidth in the axial and lateral dimensions, respectively.

2, has an azimuth beamwidth φ_{BW} , elevation beamwidth θ_{BW} and beamdepth r_{BD} . In this section, we derive the beamdepth and the maximum range limits within which the finite depth beamforming can be achieved, referred to as the EBRD for a URA. We investigate how the spatial focus region and array geometry influence the variation in beamdepth and the extent of the EBRD.

We assume a LoS channel between the UE and the BS. The near-field channel $\mathbf{h} \in \mathbb{C}^{N_{\text{BS}} \times 1}$ based on the USW model is mathematically formulated as [19]

$$\mathbf{h} = \sqrt{g}\mathbf{b}(\varphi, \theta, r), \quad (5)$$

where g denotes the channel gain taking into account the path loss and antenna gain, and r is the distance between the UE and the origin of the URA. We consider a BS equipped with a generalized URA that serves a near-field UE located at $(\varphi, \theta, r_{\text{F}})$. Let $\mathbf{w}(\varphi, \theta, z)$ denote the beamforming vector based on the conjugate phase method. The array gain \mathcal{G}_{URA} characterizes the normalized received power, and is defined as

$$\mathcal{G}_{\text{URA}} = \left| \mathbf{w}(\varphi, \theta, z)^{\text{H}} \mathbf{h}(\varphi, \theta, r_{\text{F}}) \right|^2, \quad (6)$$

$$\forall \varphi \in [-\pi/2, \pi/2], \theta \in [-\pi/2, \pi/2], z \in [2D, \infty].$$

In the subsequent analysis, we utilize (6) to derive array gain for the URA and characterize beamdepth and EBRD for different array geometries.

A. Finite Beamdepth and EBRD

We define the beamdepth, r_{BD} , as the distance interval $z \in [r_{\text{F}}^{\text{min}}, r_{\text{F}}^{\text{max}}]$ where the normalized array gain is at most 3 dB below its maximum value. The beamforming vector $\mathbf{w}(\varphi, \theta, z)$ in (6), designed using conjugate phase, achieves maximum array gain at the focal point $z = r_{\text{F}}$ and decreasing array gain at distances away from r_{F} . Then the normalized array gain in (6) achieved by $\mathbf{w}(\varphi, \theta, z)$ is given by

$$\mathcal{G}_{\text{URA}} \approx \left| \frac{1}{N_1 N_2} \sum_{n_1} \sum_{n_2} e^{j \frac{\pi}{\lambda} (n_1^2 d^2 \beta_1 + n_2^2 d^2 \beta_2) z_{\text{eff}}} \right|^2, \quad (7)$$

where $z_{\text{eff}} = \left| \frac{z - r_{\text{F}}}{z r_{\text{F}}} \right|$. Since N_{BS} is large, the summation in (7) can be approximated with a Riemann integral¹ to obtain

$$\mathcal{G}_{\text{URA}} \approx \left| \frac{1}{N_1 N_2} \int_{-\frac{N_1}{2}}^{\frac{N_1}{2}} \int_{-\frac{N_2}{2}}^{\frac{N_2}{2}} e^{j \frac{\pi}{\lambda} (n_1^2 d^2 \beta_1 + n_2^2 d^2 \beta_2) z_{\text{eff}}} dn_1 dn_2 \right|^2. \quad (8)$$

By the change of variables $x_1 = \sqrt{\frac{2n_1^2 d^2 \beta_1 z_{\text{eff}}}{\lambda}}$ and $x_2 = \sqrt{\frac{2n_2^2 d^2 \beta_2 z_{\text{eff}}}{\lambda}}$, we express the array gain in (8) in terms of Fresnel functions as

$$\mathcal{G}_{\text{URA}} = \frac{[C^2(\gamma_1) + S^2(\gamma_1)] [C^2(\gamma_2) + S^2(\gamma_2)]}{(\gamma_1 \gamma_2)^2}, \quad (9)$$

where $C(\gamma_i) = \int_0^{\gamma_i} \cos(\frac{\pi}{2} x_i^2) dx_i$ and $S(\gamma_i) = \int_0^{\gamma_i} \sin(\frac{\pi}{2} x_i^2) dx_i$ are the Fresnel functions [6], with $i \in \{1, 2\}$.

Moreover, $\gamma_1 = \sqrt{\frac{N_1^2 d^2 \beta_1}{2\lambda} z_{\text{eff}}}$ and $\gamma_2 = \sqrt{\frac{N_2^2 d^2 \beta_2}{2\lambda} z_{\text{eff}}}$. Based on the gain function in (9), we present Theorems 1 and 2 to characterize the 3 dB beamdepth and the EBRD, respectively.

Theorem 1. For a generalized URA, the 3 dB beamdepth r_{BD} obtained by focusing a beam at a distance r_{F} from the BS is given by

$$r_{\text{BD}} = \frac{8r_{\text{F}}^2 r_{\text{RD}} \alpha_{3\text{dB}} \eta (\eta^2 + 1) \sqrt{\beta_1 \beta_2}}{[\eta r_{\text{RD}} \sqrt{\beta_1 \beta_2}]^2 - [4\alpha_{3\text{dB}} r_{\text{F}} (\eta^2 + 1)]^2}. \quad (10)$$

Proof. Proof is provided in Appendix A. \square

Theorem 2. The farthest distance for a given pair of azimuth and elevation angles, at which near-field beamfocusing for a URA can be achieved, is termed the effective beamfocusing Rayleigh distance r_{EBRD} and is given by

$$r_{\text{F}} < \frac{\eta r_{\text{RD}}}{4\alpha_{3\text{dB}} (1 + \eta^2)} \sin \theta \sqrt{1 - \sin^2 \theta \sin^2 \varphi}. \quad (11)$$

Proof. Proof is provided in Appendix B. \square

The beamdepth and EBRD expressions for a uniform square array (USA) and a ULA can be derived as follows:

Corollary 1. For a USA, beamdepth $r_{\text{BD}}^{\text{USA}}$ is obtained by substituting $\eta = 1$ in (10) to get

$$r_{\text{BD}}^{\text{USA}} = \begin{cases} \frac{16r_{\text{F}}^2 r_{\text{RD}} \alpha_{3\text{dB}} \sqrt{\beta_1 \beta_2}}{(r_{\text{RD}} \sqrt{\beta_1 \beta_2})^2 - (8\alpha_{3\text{dB}} r_{\text{F}})^2}, & r_{\text{F}} < \frac{r_{\text{RD}}}{8\alpha_{3\text{dB}}} \sqrt{\beta_1 \beta_2}, \\ \infty, & r_{\text{F}} \geq \frac{r_{\text{RD}}}{8\alpha_{3\text{dB}}} \sqrt{\beta_1 \beta_2}. \end{cases} \quad (12)$$

Note that in the boresight case $\sqrt{\beta_1 \beta_2} = 1$ and $\alpha_{3\text{dB}} = 1.25$, (12) reduces to the beamdepth expression in [Eq. 23, [10]]. The boresight case of a URA was considered in [11].

Corollary 2. For a ULA along y-axis, beamdepth $r_{\text{BD}}^{\text{ULA}}$ is given by

$$r_{\text{BD}}^{\text{ULA}} = \begin{cases} \frac{8\alpha_{3\text{dB}} r_{\text{F}}^2 r_{\text{RD}} \cos^2(\varphi)}{(r_{\text{RD}} \cos^2(\varphi))^2 - (4\alpha_{3\text{dB}} r_{\text{F}})^2}, & r_{\text{F}} < \frac{r_{\text{RD}}}{4\alpha_{3\text{dB}}} \cos^2(\varphi), \\ \infty, & r_{\text{F}} \geq \frac{r_{\text{RD}}}{4\alpha_{3\text{dB}}} \cos^2(\varphi). \end{cases} \quad (13)$$

The special case of a ULA was covered in [3]. Beamdepth for uniform circular array (UCA) is derived in [20].

¹For large N_{BS} with small antenna elements, the discrete sum converges to the Riemann integral.

We evaluate the impact of the approximation in (3)(b), where the cross term is neglected, on the beamdepth expression in (10) by comparing it with the numerically computed beamdepth. The numerical beamdepth is obtained by computing the array gain using the exact array response vector in (2) and identifying the 3 dB points of the resulting gain function. As shown in Fig. 3, the analytical beamdepth closely matches the numerical results, with a slight deviation observed at very short focal distances ($< 2D$). At larger distances, this deviation vanishes as the contribution of the neglected cross term diminishes. Moreover, since the EBRD represents the maximum distance limit for beamfocusing, the approximation in (3)(b) has a negligible impact on the EBRD. Note that the EBRD is conceptually distinct from the ERD in [15]. Specifically, the ERD defines the boundary at which the beamforming loss incurred when approximating the near-field channel with a far-field model exceeds a prescribed threshold. For a ULA, the ERD is given by $0.367 r_{\text{RD}} \cos^2(\varphi)$ for a threshold of 0.05. As shown in Fig. 4, the ERD overestimates the near-field region from a beamfocusing perspective, whereas only the region within the EBRD truly supports beamfocusing.

B. Impact of Spatial Focus Region and Array Geometry

A narrower beamdepth in the near-field allows for serving more users within the same angular direction while reducing mutual interference. In the following, we analyze how both beamdepth and EBRD vary with spatial focus region and array geometry.

1) *Spatial Focus Region*: In the far-field, the beamwidth broadens as the beam is steered away from the boresight [Fig. 1, [2]]. Similarly, the beamdepth r_{BD} increases as the focal region moves farther away from the array, as indicated by the quadratic dependence on r_{F} in (10). This can also be observed from the approximate expression in (16) (Section IV-A1) and from Fig. 16 (Section VI). In the principal plane², beamdepth is minimal at the boresight and expands toward the endfire directions. For wide arrays ($\eta \gg 1$), beamdepth is primarily influenced by the azimuth angle φ , whereas for taller arrays ($\eta \ll 1$), it is mainly governed by the elevation angle θ . In the cross plane, the variation of the beamdepth is more complex as both the length and width of the aperture affect it. To exemplify, the variation of beamdepth with respect to the azimuth angle φ for different URA configurations is shown in Fig. 5, where r_{BD} increases at larger azimuth angles for wide arrays. Likewise, as the elevation angle θ increases from the boresight $\pi/2$ to endfire direction $5\pi/6$, beamdepth r_{BD} increases significantly for tall arrays. However, in the cross plane, beamdepth decreases at large elevation angles for wide arrays. A similar trend for beamwidth in the angular domain is reported in [Fig. 2, 16, [21]].

2) *Array Geometry*: For a fixed number of antenna elements $N_{\text{BS}} = N_1 N_2$, different array geometries can be realized by varying the aspect ratio $\eta = N_1/N_2$, which results in different aperture lengths given by $D = d\sqrt{N_1^2 + N_2^2}$. Alternatively, one can fix the aperture length D and vary η , allowing N_{BS} to

²For wide arrays, azimuth is considered the principal plane, whereas for tall arrays, elevation serves as the principal plane.

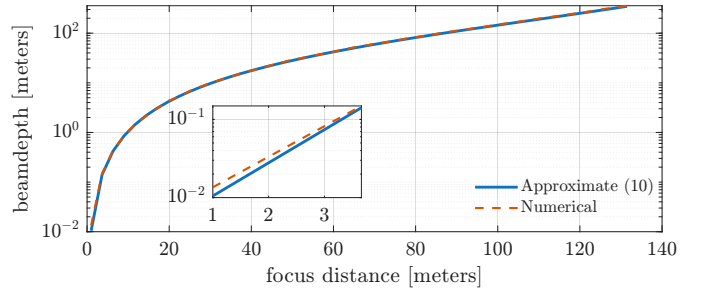


Fig. 3: Numerical and analytical beamdepth for a (256×16) URA operating at 30 GHz. The zoom inset highlights the beamdepth for focus distances less than $2D = 5$.

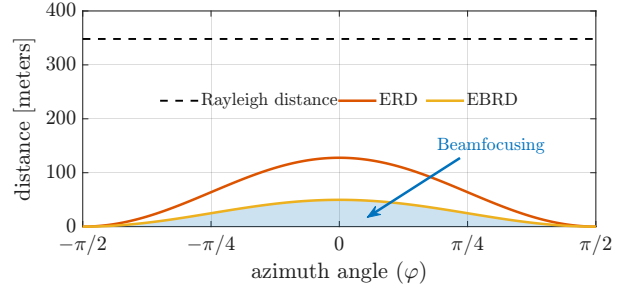


Fig. 4: Near-field boundary in terms of ERD and EBRD for a ULA. Here $f_c = 28$ GHz, $N_{\text{BS}} = 256$, $r_{\text{RD}} = 348$ m.

scale with the array shape. Furthermore, by keeping D constant and varying the operating frequency, N_{BS} can be adjusted as a function of both array geometry and wavelength. In the following analysis, we examine all three scenarios. To provide analytical insights, the beamdepth expression in (10) can be approximated for boresight transmission as

$$r_{\text{BD}} \approx \frac{8r_{\text{F}}^2 \alpha_{3\text{dB}} (\eta^2 + 1)}{\eta r_{\text{RD}}}, \quad (14)$$

where r_{F} remains the same for all the array configurations.

(i) *Fixed Number of Antenna Elements*: For a fixed number of elements $N_{\text{BS}} = N_1 N_2$, the aperture length $D = d\sqrt{N_1^2 + N_2^2}$ is minimized when the array is square, i.e., $N_1 = N_2$, corresponding to a USA. As a result, the Rayleigh distance $r_{\text{RD}} = \frac{2D^2}{\lambda}$ is minimized for square arrays and maximized for ULA configurations. Additionally, the combined term $\alpha_{3\text{dB}} \left(\frac{\eta^2 + 1}{\eta} \right)$ achieves its maximum value when $\eta = 1$, i.e., for a square URA, and diminishes for other aspect ratios. Therefore, beamdepth r_{BD} is maximized when the array is square, as shown in Fig. 6 (black curve).

(ii) *Fixed Aperture Length*: For a fixed aperture length D , the Rayleigh distance r_{RD} remains constant across different aspect ratios. However, the composite factor $\alpha_{3\text{dB}} \left(\frac{\eta^2 + 1}{\eta} \right)$, which directly influences beamdepth, reaches its maximum for a square array. However, as shown in Fig. 6 (blue curve), the variation of beamdepth with respect to η is less significant under a fixed aperture length than in the fixed element count scenario. This is because r_{RD} —being relatively large in magnitude—dominates the beamdepth expression (14), making the influence of the geometry-dependent factor $\alpha_{3\text{dB}} \left(\frac{\eta^2 + 1}{\eta} \right)$ comparatively minor.

Extending the Giga-MIMO example discussed in Section I,

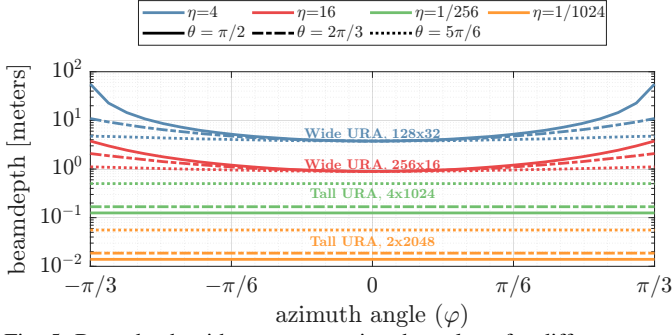


Fig. 5: Beamdepth with respect to azimuth angle φ for different array configuration η and elevation angle θ .

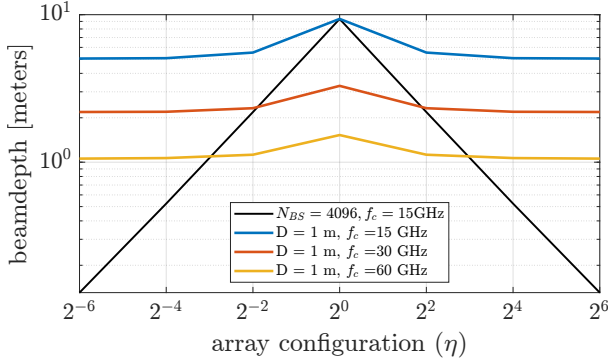


Fig. 6: Beamdepth with respect to η for fixed number of antenna elements N_{BS} and aperture length D .

we further analyze the impact of the operating frequency on the beamdepth under a fixed aperture length D . Fig. 6 presents the simulated beamdepth behavior for $D = 1$ m when the carrier frequency increases from 15 GHz to 60 GHz. The results demonstrate a clear decrease in beamdepth with increasing frequency. This trend is consistent with the approximation in (14), where the Rayleigh distance r_{RD} increases with frequency (due to the corresponding decrease in wavelength), thereby reducing the beamdepth even for a fixed aperture length.

3) *Limits of Beamfocusing*: The EBRD defines the near-field boundary beyond which beamfocusing becomes infeasible. Within the EBRD boundary, beamfocusing enables serving multiple users in the same angular direction, thereby enhancing multiuser capacity. It is therefore important to investigate methods for enlarging the EBRD. We first analyze the case with a fixed element count, followed by the case with a fixed aperture length.

(i) *Fixed Number of Antenna Elements*: Based on (11), since the Rayleigh distance r_{RD} is minimal for a square URA, and it dominates the other factor as explained earlier, the EBRD is smallest for square URA and increases as the URA geometry transitions toward a ULA. This relationship is illustrated in Fig. 7, where the EBRD is plotted with respect to azimuth angle φ , and as a function of η and elevation angle θ . Additionally, the EBRD for wide arrays varies with the azimuth angle, while for tall arrays, it depends on the elevation angle. For all configurations in the principal plane, the EBRD reaches its maximum at the boresight direction ($\varphi = 0, \theta = \pi/2$) and decreases in the endfire directions. The largest EBRD is observed for the URA configuration with $\eta = 0.004$,

while the smallest EBRD is associated with the square URA configuration ($\eta = 1$). Note that the EBRD for $\eta = 0.016$ and $\eta = 0.004$ remains constant with respect to the azimuth angle φ , as these configurations represent tall URAs ($\eta \ll 1$). Furthermore, for these tall arrays, the EBRD decreases further when the elevation angle deviates from the boresight ($\theta = \pi/2$).

(ii) *Fixed Aperture Length*: For a fixed aperture length, the square array continues to exhibit the lowest EBRD, while the variation in EBRD across different array geometries becomes less pronounced—consistent with the beamdepth behavior discussed earlier. Building on this, we now fix the array geometry and investigate how the EBRD scales with aperture length D and operating frequency. The objective is to identify the dominant factor that drives the expansion of the EBRD region, thereby identifying the array geometries enabling more users to benefit from near-field communication.

To this end, we evaluate EBRD as a function of azimuth angle for varying aperture sizes and carrier frequencies as shown in Fig. 8. At $D = 1$ m—which approximates the physical dimensions of the Giga-MIMO array—EBRD at boresight reaches approximately 13 m at 15 GHz. Increasing the frequency to 60 GHz extends the EBRD to around 55 m, though this increase may still be modest. In contrast, increasing the aperture length offers a more significant impact: as shown in Fig. 8, the EBRD reaches approximately 123 m at 15 GHz when D is increased to 3 m. This dominant effect of aperture size over frequency can be attributed to the scaling behavior of the Rayleigh distance $r_{RD} = \frac{2D^2}{\lambda}$, which increases quadratically with D but only linearly with wavelength. Thus, enlarging the aperture length seems to be a more effective strategy for substantially expanding the near-field region.

C. Multiuser Capacity Analysis

In this subsection, we present numerical examples to evaluate multiuser capacity with respect to the EBRD and the array geometry. We consider a hybrid beamformer with analog precoder \mathbf{W} . Additionally, zero-forcing is applied as the digital precoder. The overall spectral efficiency (SE) is given by

$$R = \sum_{m=1}^5 \log_2 \left(1 + \frac{p_m |\mathbf{h}_m^H \mathbf{W} \mathbf{f}_m|^2}{\sigma_m^2 + \sum_{l \neq m} p_l |\mathbf{h}_m^H \mathbf{W} \mathbf{f}_l|^2} \right), \quad (15)$$

where p_m denotes power allocated to the m^{th} user and σ_m^2 denotes the noise variance. Furthermore, \mathbf{f}_m represents the m^{th} column of the digital precoder.

1) *SE vs. EBRD*: Finite beamdepth is achievable only within the EBRD region, limiting spatial multiplexing gains due to beamdepth to the near-field region bounded by the EBRD. To illustrate this, we consider a 64×8 URA serving five users positioned in the boresight direction ($\varphi = 0, \theta = \pi/2$). Users are distributed uniformly across three distinct regions: the EBRD region $[2D, r_{EBRD}]$, the near-field region beyond EBRD $[r_{EBRD}, r_{RD}]$, and the far-field region $[r_{RD}, 100r_{RD}]$. We employ both polar and discrete Fourier transform (DFT) codebooks for each of these scenarios. The resulting SE is shown in Fig. 9. Within the EBRD region, the polar codebook achieves a SE of 5.8 bps/Hz, compared to only 2 bps/Hz with the DFT codebook. Additionally, SE is similar for both codebooks in

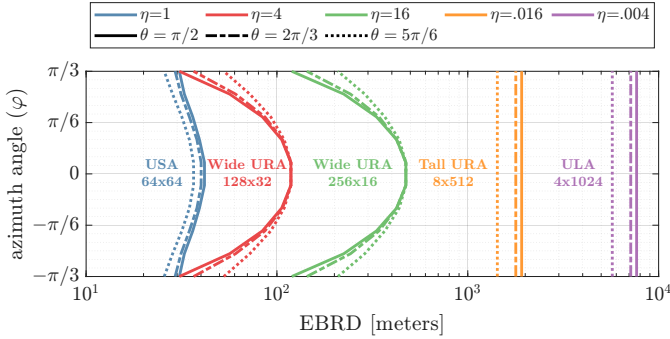


Fig. 7: Finite beamdepth limit in terms of EBRD with respect to azimuth angle for different array configurations and elevation angles.

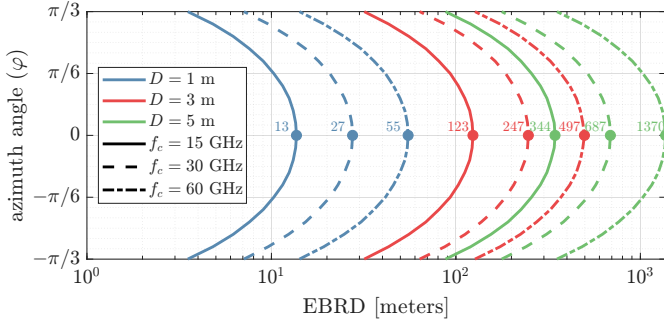


Fig. 8: Finite beamdepth limit in terms of EBRD with respect to azimuth angle for different aperture lengths and frequencies.

the near-field region outside the EBRD and in the far-field. It is important to emphasize that the EBRD determines the near-field boundary in terms of multiplexing gain when UEs are distributed linearly along a single angular direction in the range domain. For uniformly distributed UEs, regions outside the EBRD may still achieve slightly higher SE than the far-field case, owing to the improved lateral resolution at shorter distances compared to the far-field.

2) *SE vs. Array Geometry*: Array geometry governs both beamdepth and the EBRD; however, its impact diminishes under a fixed aperture length constraint. Nonetheless, under both fixed-element and fixed-aperture scenarios, elongated array configurations like ULA yield the smallest beamdepth and the largest EBRD, thereby enhancing spatial multiplexing.

To quantify the impact of array geometry, we evaluate the SE, as depicted in Fig. 10, across $\eta = [1, 4, 16]$, under two constraints: fixed aperture length D and fixed number of elements N_{BS} . As a baseline, the square URA configuration ($\eta = 1$) is used, which is expected to yield the lowest SE due to its wider beamdepth and limited EBRD. In all scenarios, five users are randomly distributed along the boresight direction within the range $[2D, r_{EBRD}]$, where r_{EBRD} varies with array geometry.

Under the fixed-element constraint ($N_{BS} = 1024$), SE increases consistently with η , i.e., from $\eta = 1$ to $\eta = 16$, across all signal-to-noise ratio (SNR) values. This trend aligns with Fig. 6 (black curve), where a reduction in beamdepth with increasing η (i.e., transitioning toward a ULA) mitigates inter-user interference and enhances SE.

Under the fixed-aperture constraint ($D = 2$), the SE trend is more interesting. While the configuration with $\eta = 4$ achieves

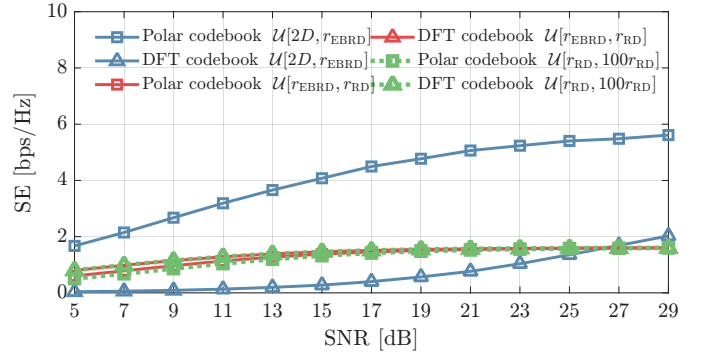


Fig. 9: The comparison of SE versus SNR, with respect to user distribution.

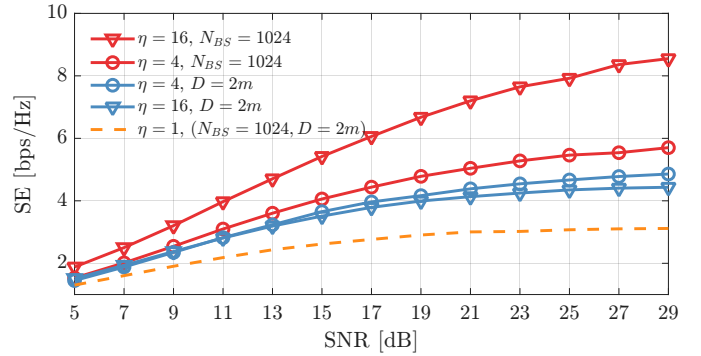


Fig. 10: The comparison of SE versus SNR, with respect to array configurations.

higher SE than $\eta = 1$, the SE for $\eta = 16$ drops compared to $\eta = 4$. This behavior can be explained by the SE expression in (15), where the numerator is influenced by the beamforming gain, dependent on the number of antenna elements, and the denominator reflects mutual interference. Since beamdepths for $\eta = 4$ and $\eta = 16$ are nearly identical (as shown in Fig. 6), the variation in SE arises primarily from the reduced element count in the $\eta = 16$ configuration, which diminishes the beamforming gain and thereby reduces the overall SE.

IV. AXIAL VS. LATERAL BEAM PATTERN ANALYSIS

Beam resolution is key to maximizing wireless communication capacity by enabling precise user separation and minimizing interference. In the near-field, beams can be focused in both the axial (range) and lateral (angular) dimensions, making it instructive to analyze and compare beam patterns in these dimensions. In the subsequent analysis, we examine the beam resolution, as well as the sidelobe patterns, in both the axial and lateral dimensions to provide a comparative analysis and implications for near-field wireless communication.

A. Beam Resolution

Axial and lateral resolution are determined by the beamdepth and beamwidth, respectively. For tractability, we compare beamdepth and beamwidth of a ULA at a fixed distance r_f . Specifically, we consider a ULA with boresight transmission, where $\alpha_{3dB} = 1.75$ for $\varphi = 0^\circ$.

1) *Axial Resolution*: For this configuration, the denominator in (13) is simplified to $(r_{\text{RD}}^2 - 49r_{\text{F}}^2)$. A finite value of $r_{\text{BD}}^{\text{ULA}}$ is attained only when $r_{\text{F}} < \frac{r_{\text{RD}}}{7}$, ensuring that r_{RD}^2 remains significantly larger than $49r_{\text{F}}^2$. Consequently, we can neglect the $49r_{\text{F}}^2$ term and substitute $r_{\text{RD}} = \frac{2D^2}{\lambda}$ in (13), yielding the following simplified expression for beamdepth of a ULA:

$$r_{\text{BD}}^{\text{ULA}} \approx 7\lambda \left(\frac{r_{\text{F}}}{D}\right)^2. \quad (16)$$

2) *Lateral Resolution*: The 3 dB beamwidth for N_{BS} element ULA can be approximated as $\varphi_{\text{BW}} \approx \frac{\lambda}{N_{\text{BS}}d \cos(\varphi)}$ [22]. Furthermore, lateral range resolution Δr_{az} in the azimuth direction is given by [23]

$$\Delta r_{\text{az}} \approx r_{\text{F}} \varphi_{\text{BW}}. \quad (17)$$

The lateral resolution based on the beamwidth φ_{BW} at $\varphi = 0^\circ$ can be obtained from (17) as

$$\Delta r_{\text{az}}^{\text{ULA}} \approx \lambda \left(\frac{r_{\text{F}}}{D}\right), \quad (18)$$

where $D = N_{\text{BS}}d$ represents aperture of the ULA here. In the radiative near-field $r_{\text{F}} > 2D$, therefore, the factor $\frac{r_{\text{F}}}{D} > 1$.

3) *Comparative Analysis*: Comparing (16) with (18), $\Delta r_{\text{az}}^{\text{ULA}}$ yields finer resolution compared to the $r_{\text{BD}}^{\text{ULA}}$ that denotes the axial resolution. Therefore, for a given distance r_{F} , the range resolution in the lateral dimensions is consistently higher than that in the axial dimension. Notably, $r_{\text{BD}}^{\text{ULA}}$ varies quadratically with the factor $\frac{r_{\text{F}}}{D}$, while $\Delta r_{\text{az}}^{\text{ULA}}$ varies linearly. Therefore, as r_{F} is increased, axial resolution degrades more rapidly than the lateral resolution, until EBRD is reached, after which axial resolution capability is completely lost. Finally, it is pertinent to emphasize that lateral resolution is further enhanced in the near-field due to proximity, as the values of r_{F} in $\Delta r_{\text{az}}^{\text{ULA}}$ are smaller in the near-field compared to those in the far-field.

Extending the comparative analysis to planar arrays, we consider a URA, which provides lateral resolution along both azimuth and elevation. For a ULA, the array length coincides with the aperture and determines both the lateral and axial resolutions. In contrast, for a URA, the axial resolution is governed by the maximum array extent (aperture length), while the lateral resolution depends independently on the array extent along each dimension. Similar to (16), the axial resolution of a URA can be obtained by substituting $r_{\text{RD}} = \frac{2D^2}{\lambda}$ into (14), yielding $r_{\text{BD}}^{\text{URA}} \approx 4\lambda \left(\frac{r_{\text{F}}}{D}\right)^2 \frac{\alpha_{3\text{dB}}(\eta^2 + 1)}{\eta}$. The lateral resolution along each dimension is set by the array extent: azimuth by $D_y = N_1 d_y$ and elevation by $D_z = N_2 d_z$. Consequently, the lateral resolution in azimuth or elevation follows the same expression as in (18), with D replaced by the array length along the respective dimension. More generally, for the lateral resolution along a specific dimension D_i , $i \in \{y, z\}$, to exceed the axial resolution, the condition $\Delta r_{\text{az}}^{\text{URA}} < r_{\text{BD}}^{\text{URA}}$ must be satisfied, which leads to

$$\frac{D^2}{D_i} < \frac{4r_{\text{F}} \alpha_{3\text{dB}}(\eta^2 + 1)}{\eta}. \quad (19)$$

To illustrate the utility of (19), we consider a USA with $\eta = 1$, $\alpha_{3\text{dB}} = 1.25$, and $D = \sqrt{2}D_i$. Substituting these values yields the condition $r_{\text{F}} > \frac{D}{7}$, indicating that when the focal distance exceeds $\frac{D}{7}$, the lateral resolution of a USA surpasses the axial resolution. Notably, the minimum distance for USW operation

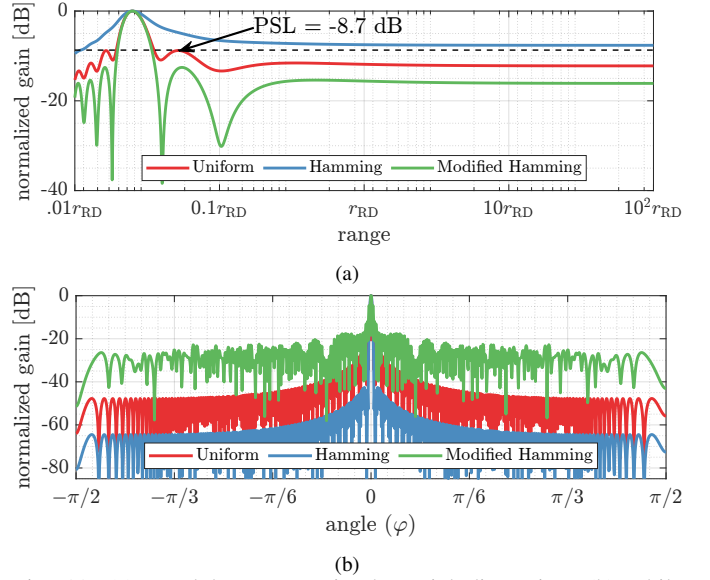


Fig. 11: (a) Forelobes appear in the axial dimension, (b) while sidelobes are observed in the lateral dimension. Applying Hamming weights reduces the sidelobes in the lateral pattern, whereas modified Hamming weights suppress the forelobes in the axial pattern.

in the near-field is $2D$, implying that this condition is always satisfied in the radiative near-field. Following a similar analysis for elongated URAs, it can be shown that at distances greater than $2D$, the lateral resolution remains superior to the axial resolution in the principal plane. However, in the cross-plane, the dimension with superior resolution is determined by the ratio of the aperture length to the array width or height.

B. Sidelobe Levels

The array gain for a ULA in the angular domain is $\mathcal{A}(u) = \left| \frac{\sin\left(\frac{N_{\text{BS}}u}{2}\right)}{N_{\text{BS}} \sin\left(\frac{u}{2}\right)} \right|^2$, where $u = v d \sin(\varphi)$ [Eq. 12, [18]], while in the range-domain it is $\mathcal{G}(\gamma) = \left| \frac{C^2(\gamma) + S^2(\gamma)}{\gamma^2} \right|$ [3]. In the near-field region, the focused beam exhibits both lateral sidelobes and axial forelobes. The peak sidelobe level (PSL) represents the highest sidelobe amplitude relative to the main-lobe peak, indicating robustness against nearby narrowband interference. In the angular domain, the PSL approximately occurs at $u \approx \frac{3\pi}{N_{\text{BS}}}$, yielding $\text{PSL}_{\text{ang}} \approx 10 \log_{10} \left(\frac{1}{3\pi/2} \right)^2 \approx -13.46$ dB, where a *small angle* approximation is applied to obtain $\sin\left(\frac{3\pi}{2N_{\text{BS}}}\right) \approx \frac{3\pi}{2N_{\text{BS}}}$. In the range domain, solving numerically $\frac{d}{d\gamma} \left(\frac{C^2(\gamma) + S^2(\gamma)}{\gamma^2} \right) = 0$ yields $\gamma_{\text{PSL}} \approx 2.28$ with $10 \log_{10}(\mathcal{G}(\gamma_{\text{PSL}})) \approx -8.7$ dB. Note that the PSL along the axial dimension is higher than that along the lateral dimension. Hence, suppression of axial forelobes may be more critical for mitigating interference.

Standard far-field techniques typically apply amplitude tapering distribution $\mathbf{f}(n)$ in the array domain as $\mathbf{b}(\varphi, r) \odot \mathbf{f}(n)$, to reduce the sidelobe levels in the angular domain. It may be desirable to utilize the same amplitude distribution functions to reduce axial forelobes as well. However, directly using these functions amplifies the forelobes in the axial dimension, since the Fresnel function in the range domain is quadratic in n and introduces angular spreading. Here, we present a transformation

that maps the standard far-field window $\mathbf{f}(n)$ to a modified window $\mathbf{g}(n)$, thereby allowing existing window designs to be directly adapted for the suppression of axial forelobes.

Theorem 3. Given a far-field window function $\mathbf{f}(n)$ designed to attenuate angular sidelobes, a corresponding distribution $\mathbf{g}(n)$ can be derived to suppress axial forelobes, via the transformation:

$$\mathbf{g}(n) = |n| \mathbf{f}(n^2), \quad (20)$$

Proof. The proof is inspired by [24] and is in Appendix C. \square

To demonstrate the application of (20), Fig. 11 compares the axial and lateral beam patterns for three window designs: (i) uniform (untapered) case, (ii) conventional Hamming window $\mathbf{f}(n)$, and (iii) modified Hamming window $\mathbf{g}(n)$ obtained via (20). The analysis considers a 256-element ULA operating at 28 GHz, focused at $r_f = r_{\text{rd}}/40$ and $\varphi = 0^\circ$ in the near-field region. It is important to note that (20) can be applied to other window functions as well; the Hamming window is chosen here for illustration purposes, and is expressed as [25]

$$\mathbf{f}(n) = 0.54 - 0.46 \cos\left(\frac{2\pi n}{N_{\text{BS}} - 1}\right), \quad 0 \leq n \leq N_{\text{BS}} - 1. \quad (21)$$

Furthermore, the modified Hamming distribution is obtained by transforming $\mathbf{f}(n)$ to $\mathbf{g}(n)$ according to (20). Then the amplitude distribution $\mathbf{g}(n)$ is applied to the near-field array response vector as

$$\mathbf{b}(\varphi, r) = \mathbf{b}(\varphi, r) \odot \mathbf{g}(n). \quad (22)$$

In Fig. 11, the conventional Hamming distribution reduces lateral sidelobes but increases the axial forelobes. The modified Hamming $\mathbf{g}(n)$ reduces the axial forelobes from -8.7 dB to -13 dB, but raises the lateral sidelobes. The desired amplitude distribution to suppress the axial forelobes degrades the angular pattern by increasing the lateral sidelobes, and vice versa. Therefore, achieving low sidelobe levels in both axial and lateral dimensions requires a suitable compromise between the two. Moreover, while the conventional Hamming window broadens the beamwidth, the modified Hamming window primarily increases the beamdepth without affecting the beamwidth. Beam broadening of the mainlobe occurs only when energy is redistributed from the sidelobes into the mainlobe. Since the modified Hamming window does not suppress sidelobe energy in the lateral dimension, no lateral energy redistribution occurs, and thus the beamwidth and lateral resolution remain unchanged.

The overall lateral beam pattern is governed by the product of the antenna element pattern and the array factor; consequently, both the achievable beamwidth and the lateral sidelobe levels of the array are also affected by the beamwidth and sidelobe characteristics of the individual antenna elements. This principle, however, does not extend to the axial dimension. Beamdepth is not an intrinsic electromagnetic property of a single antenna element, and therefore, axial forelobes cannot be mitigated through element-level design. To simultaneously suppress sidelobes in both the axial and lateral domains, one can formulate an optimization problem that maximizes the two-dimensional mainlobe energy relative to the sidelobe energy of

the beam pattern. This leads to an energy concentration formulation, whose solution is obtained via a generalized eigenvalue problem [26]. As an alternative, sidelobe reduction may also be achieved using iterative projection-based techniques, such as the Gerchberg–Saxton algorithm applied in the polar domain [27].

V. SPATIAL DEGREES OF FREEDOM

Given a LoS MIMO channel $\mathbf{H} \in \mathbb{C}^{N_t \times N_r}$ with N_t transmit and N_r receive antennas, the spatial DoF denote the number of independent sub-channels that support parallel communication modes. Mathematically, this corresponds to the number of non-zero singular values from the singular value decomposition (SVD) of \mathbf{H} , or equivalently, the rank of the Gramian matrix $\mathbf{R} = \mathbf{H}^H \mathbf{H}$. For a far-field LoS MIMO channel, the rank is one; however, a higher rank can be achieved by leveraging the radiative near-field region. It is important to note that channel capacity depends not only on the rank but also on the condition number of \mathbf{H} , which ideally equals one. Consequently, the EDoF is employed in practice to quantify the number of useful sub-channels at high SNR, where multiple EDoF contribute to capacity. Having many EDoF is only beneficial if the SNR is sufficiently large to exploit them. In contrast, at low SNR, channel capacity is dominated by the largest singular value, and a rank-one channel is preferable.

In this section, we first review existing metrics for EDoF. We then formulate a new expression for EDoF tailored to the URA, characterizing its dependence on distance and angle. Finally, we provide comparisons across different URA configurations and establish the boundary where the EDoF reduces to one.

In practice, the singular values of \mathbf{H} remain approximately constant up to a certain index, beyond which they decay rapidly toward zero. This transition index is defined as the EDoF [28], expressed as $\sigma_1 \approx \sigma_2 \approx \dots \approx \sigma_{\text{EDoF}} \gg \sigma_{\text{EDoF}+1} > \dots > \sigma_{\text{DoF}}$. Accordingly, $\text{tr}(\mathbf{R}) = \sum_{n=1}^{\text{DoF}} \sigma_n^2 \approx \text{EDoF} \times \sigma_{\text{EDoF}}^2$, and $\|\mathbf{R}\|_{\text{F}}^2 = \sum_{n=1}^{\text{DoF}} \sigma_n^4 \approx \text{EDoF} \times \sigma_{\text{EDoF}}^4$. By combining these two relations, the EDoF can be approximated as

$$\text{EDoF}_1 \approx \frac{(\sum_{n=1}^{\text{DoF}} \sigma_n^2)^2}{\sum_{n=1}^{\text{DoF}} \sigma_n^4} = \frac{\text{tr}^2(\mathbf{R})}{\|\mathbf{R}\|_{\text{F}}^2}, \quad (23)$$

which quantifies the number of dominant singular values and thus, the effective number of useful sub-channels. Although compact in form, this expression does not directly reveal how EDoF vary with distance and angle in the near-field region.

A. Effective Spatial Degrees of Freedom

The DoF correspond to the number of independent columns, whereas the EDoF represent the set of mutually orthogonal columns in \mathbf{H} . Our proposed approach transforms \mathbf{H} into the angular domain via the DFT to identify the set of orthogonal sub-channels. In this domain, the EDoF can be interpreted as the number of distinguishable transmit beams observable at the receiver. From a geometric perspective, it can further be approximated as the ratio between the receive aperture length D_r and the 3 dB beamwidth of the transmit array given in (18). Consequently, the EDoF is expressed as

$$\text{EDoF}_2 \approx \frac{D_r}{\frac{\lambda_r}{D_t}} = \frac{D_r D_t}{\lambda_r}. \quad (24)$$

The above expression is also derived in [29] based on optical diffraction theory. Direct computation of the DFT of \mathbf{H} is intractable due to the coupling among the DoF of the MIMO channel. To address this, we first estimate the EDoF based solely on the transmit array and subsequently rescale the result by the receive aperture length. This formulation is motivated by (24), where the EDoF for a unit-length aperture is first obtained from the transmit beamwidth and then scaled by D_r . In the following, we describe the proposed procedure for computing the EDoF based on the transmit array.

The spherical wavefront can be viewed as a weighted sum of planar wavefronts. More specifically, the near-field array response vector in (2) can be degenerated into a series of DFT beams [7]. For a URA, orthogonal DFT beams can be obtained by uniformly sampling the directional cosines u_y and u_z as

$$u_y^{(n_1)} = \sin \theta_{n_1} \sin \varphi_{n_1} = -\frac{n_1 \lambda}{2N_1 d}, \quad (25a)$$

$$u_z^{(n_2)} = \cos \theta_{n_2} = -\frac{n_2 \lambda}{2N_2 d}. \quad (25b)$$

where $(u_y^{(n_1)}, u_z^{(n_2)})$ represent spatial frequency resource for a URA. Furthermore, to ensure that the sampled spatial frequencies correspond to physically realizable propagating waves, u_y and u_z must be real-valued and lie within the visible region, satisfying the unity constraint $\sqrt{u_y^2 + u_z^2} \leq 1$ [30]. The $(n_1, n_2)^{\text{th}}$ element of the DFT vector can be represented as

$$\mathbf{a}_{\text{URA}}(u_y^{(n_1)}, u_z^{(n_2)}) = e^{j\nu(n_1 d u_y^{(n_1)} + n_2 d u_z^{(n_2)})}. \quad (26)$$

We compute the gain function $f(u_y^{(n_1)}, u_z^{(n_2)}; \varphi, \theta, r_F)$ associated with each spatial frequency $(u_y^{(n_1)}, u_z^{(n_2)})$ by computing the DFT coefficients for the near-field response vector $\mathbf{b}_{\text{URA}}^H(\varphi, \theta, r_F)$ as given in (27).

Theorem 4. For a URA, the normalized gain function $f(u_y^{(n_1)}, u_z^{(n_2)}; \varphi, \theta, r_F)$ can be approximated in terms of Fresnel functions as

$$\tilde{f}(u_y^{(n_1)}, u_z^{(n_2)}; \varphi, \theta, r_F) \approx \frac{\mathcal{G}_1(\gamma_1, \gamma_2) \mathcal{G}_2(\gamma_3, \gamma_4)}{16\gamma_2\gamma_4}, \quad (28)$$

where

$$\begin{aligned} \gamma_1 &= (u_y^{(n_1)} - u_y) \sqrt{\frac{r_F}{d(1-u_y^2)}}, \gamma_2 = \frac{N_1}{2} \sqrt{\frac{d(1-u_y^2)}{r_F}}, \\ \gamma_3 &= (u_z^{(n_2)} - u_z) \sqrt{\frac{r_F}{d(1-u_z^2)}}, \gamma_4 = \frac{N_2}{2} \sqrt{\frac{d(1-u_z^2)}{r_F}}. \end{aligned} \quad (29)$$

$$\begin{aligned} f(u_y^{(n_1)}, u_z^{(n_2)}; \varphi, \theta, r_F) &\triangleq \left| \mathbf{b}_{\text{URA}}^H(\varphi, \theta, r_F) \mathbf{a}_{\text{URA}}(u_y^{(n_1)}, u_z^{(n_2)}) \right|^2, \\ &\approx \left| \frac{1}{N_1 N_2} \sum_{n_1} \sum_{n_2} e^{-j\frac{2\pi}{\lambda} \left(-n_1 d u_y - n_2 d u_z + \frac{n_1^2 d^2}{2r_F} \beta_1 + \frac{n_2^2 d^2}{2r_F} \beta_2 \right)} e^{j\frac{2\pi}{\lambda} (n_1 d u_y^{(n_1)} + n_2 d u_z^{(n_2)})} \right|^2, \\ &\approx \left| \frac{1}{N_1} \sum_{-N_1/2}^{N_1/2} e^{-j\pi \left(-n_1 (u_y - n_1 u_y^{(n_1)}) + \frac{n_1^2 d}{2r_F} \beta_1 \right)} \frac{1}{N_2} \sum_{-N_2/2}^{N_2/2} e^{-j\pi \left(-n_2 (u_z - n_2 u_z^{(n_2)}) + \frac{n_2^2 d}{2r_F} \beta_2 \right)} \right|^2. \end{aligned} \quad (27)$$

Moreover, $\mathcal{G}_1(\gamma_1, \gamma_2) = [C(\gamma_1 + \gamma_2) - C(\gamma_1 - \gamma_2)]^2 + [S(\gamma_1 + \gamma_2) - S(\gamma_1 - \gamma_2)]^2$ and $\mathcal{G}_2(\gamma_3, \gamma_4) = [C(\gamma_3 + \gamma_4) - C(\gamma_3 - \gamma_4)]^2 + [S(\gamma_3 + \gamma_4) - S(\gamma_3 - \gamma_4)]^2$, where $C(\cdot)$ and $S(\cdot)$ are the Fresnel integrals, defined as $C(x) = \int_0^x \cos(\frac{\pi}{2} t^2) dt$ and $S(x) = \int_0^x \sin(\frac{\pi}{2} t^2) dt$.

Proof. Proof is provided in Appendix D. \square

Given user location (φ, θ, r_F) , the gain function $\tilde{f}(u_y^{(n_1)}, u_z^{(n_2)}; \varphi, \theta, r_F)$ in (28) depends on $(u_y^{(n_1)}, u_z^{(n_2)})$. Note that $u_y^{(n_1)}$ and $u_z^{(n_2)}$ are contained in γ_1 and γ_3 respectively. Furthermore, $\mathcal{G}_1(\gamma_1) = \mathcal{G}_1(-\gamma_1)$ and $\mathcal{G}_2(\gamma_3) = \mathcal{G}_2(-\gamma_3)$. To characterize the bandwidth of spatial frequencies, we adopt the 3 dB threshold criterion. The 3 dB criterion is consistent with the conventional 3 dB definitions of beamwidth [19] and beamdepth [10]. This threshold ensures that the retained spatial paths correspond to sufficiently strong and physically meaningful propagation modes. Moreover, the concept can be easily extended to an x -dB criterion for other values of x . Alternative thresholds may affect the absolute numerical value of the EDoF; however, the qualitative trends and the relative comparisons across different array geometries remain unchanged, as presented herein. We count the spatial frequencies with the normalized gain above 0.5 and term it as the EDoF given by

$$\text{EDoF}_3(\varphi, \theta, r_F) = \sum_{n_1} \sum_{n_2} \mathbf{1} \left\{ \tilde{f}(u_y^{(n_1)}, u_z^{(n_2)}; \varphi, \theta, r_F) \geq \frac{1}{2} \right\}. \quad (30)$$

where $\mathbf{1}(\cdot)$ denotes the indicator function. For a far-field UE, a single peak value for \tilde{f} is obtained. In contrast, for a near-field UE, significant gain values for multiple spatial frequencies are observed around the user's spatial angles (u_y, u_z) . The EDoF_3 is derived from a DFT-based representation and therefore offers a coarse spatial resolution. To enhance the resolution, EDoF_3 can be computed numerically using an oversampled FFT of size $\mathcal{K}N_{\text{BS}}$, where \mathcal{K} denotes the oversampling factor. The resulting EDoF is then normalized by \mathcal{K} to compensate for the oversampling. We will now analyze (30) with respect to the focus region and array configuration.

1) *EDoF vs. Focus Region:* To gain further insight, we plot the EDoF as a function of near-field communication ranges for a ULA at $r_F \in [2D, \frac{r_{\text{RD}}}{7}]$ and azimuth angles $\varphi \in [-\pi/2, \pi/2]$, as shown in Fig. 12. The maximum EDoF is observed when the user's range is $r_F = 2D$ at the boresight angle $\varphi = 0$. The EDoF decreases monotonically as the communication distance increases. Similarly, the EDoF diminish as the user's azimuth

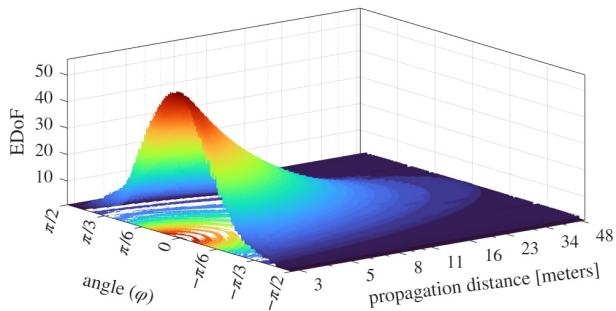


Fig. 12: EDoF for a ULA with respect to near-field communication distance and angle.

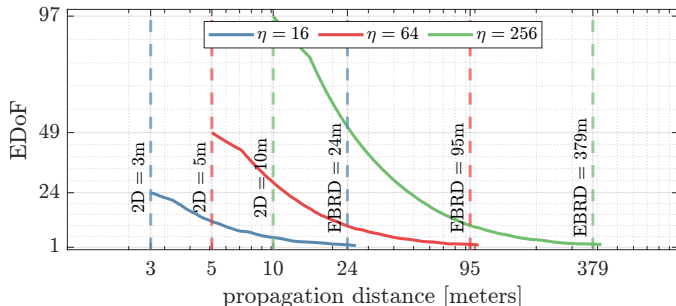


Fig. 13: EDoF versus near-field communication distance for different array configurations.

angle moves away from the boresight. The minimum EDoF, equal to one, occurs at $\frac{r_{RD}}{7} \cos^2 \varphi$, where $r_{RD} = 35$ m. Therefore, while considering the transmit array only, the EBRD given in (11) represents the boundary beyond which the EDoF in the near-field and far-field become equivalent.

2) *EDoF vs. Array Configuration*: The array configuration has a significant impact on the EDoF. To illustrate this, Fig. 13 plots the EDoF versus the user range for four array configurations, $\eta \in \{16, 64, 256\}$, with $N_t = 1024$. For $r_F < 2D$, the EDoF remains constant and equals the value at $2D$. Two important insights are worth noting here: (i) the EDoF is maximized for a URA with $\eta = 256$ and minimized for a more square configuration with $\eta = 16$, and (ii) for each configuration, the minimum EDoF occurs at the EBRD boundary, indicated by the vertical dashed lines.

B. EDoF for MIMO and Capacity Analysis

In this subsection, we present the rescaling of EDoF for MIMO and compare it with existing EDoF formulations. To account for the receive aperture D_r , we combine (30) and (24) to obtain the following expression for the scaled distance \hat{r}

$$\hat{r} = \frac{D_r D_t}{\lambda \text{EDoF}_3}. \quad (31)$$

Furthermore, the Rayleigh distance for MIMO systems depends on both D_t and D_r . We consider the following three expressions to characterize the MIMO Rayleigh distance:

$$r_{RD1} = \frac{D_t D_r}{\lambda}, \quad (32)$$

$$r_{RD2} = \frac{2(D_t + D_r)^2}{\lambda}, \quad (33)$$

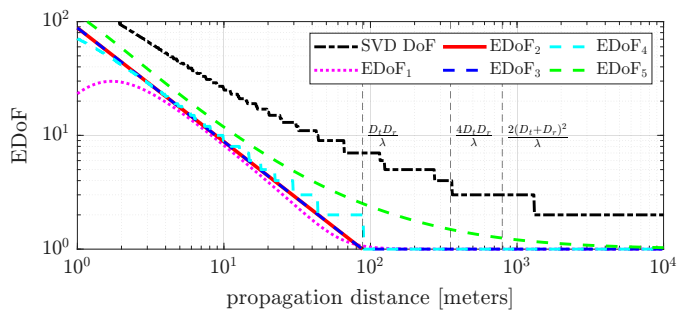


Fig. 14: EDoF of a MIMO system with a 256×16 URA at the transmitter and a 128×8 URA at the receiver, and $f_c = 28$ GHz.

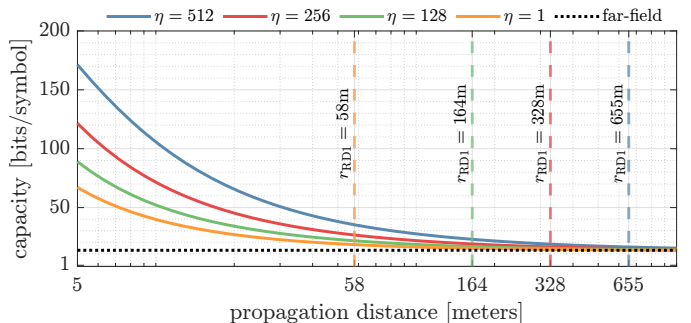


Fig. 15: Comparison of LoS MIMO channel capacity versus propagation distance for different array configurations.

$$r_{RD3} = \frac{4D_t D_r}{\lambda}, \quad (34)$$

where (32) is presented in [22], (33) is based on the maximum allowable phase error of $\pi/8$ [31], and (34) is derived from the condition that the phase discrepancy between the near-field MIMO channel and the channel modeled by the product of near-field array response vectors does not exceed $\pi/8$ [32]. Out of these three metrics, we aim to identify the boundary at which the EDoF for a MIMO configuration reduces to one. To this end, Fig. 14 plots the EDoF with respect to the propagation distance. In addition to the existing and the proposed EDoF expressions, two alternative EDoF formulations are derived from the singular values \mathbf{s}_n of \mathbf{H} . First, by normalizing the singular values as $\mathbf{q}_n = \mathbf{s}_n / \max(\mathbf{s})$, we obtain $\text{EDoF}_4 = \sum \mathbf{1}(\mathbf{q}_n > 0.5)$, which corresponds to a hard-thresholding criterion. Second, by normalizing with the sum, $\mathbf{p}_n = \mathbf{s}_n / \sum \mathbf{s}_n$, the EDoF is computed using the entropy-based definition, $\text{EDoF}_5 = \exp(-\sum \mathbf{p}_n \log(\mathbf{p}_n))$, which reflects a soft-thresholding with $\text{EDoF}_5 \in \mathbb{R}^+$, whereas in contrast we obtain integer-valued $\text{EDoF}_4 \in \mathbb{Z}^+$. As shown in Fig. 14, the DoF based on the SVD tends to overestimate EDoF and serves as an upper bound. This is because the SVD-based DoF reflects the algebraic rank of the channel and counts even weak spatial modes. In contrast, EDoF_3 accounts only for energy-dominant and physically resolvable modes, yielding a smaller yet more realistic estimate. The proposed EDoF_3 and all other EDoF definitions, except EDoF_5 , converge to one at the r_{RD1} boundary, while r_{RD2} and r_{RD3} overestimate the near-field extent in terms of EDoF. Since the proposed EDoF_3 and existing EDoF definitions converge to one at the r_{RD1} boundary, we conclude that r_{RD1} provides the most consistent criterion for the distance at which the EDoF effectively reduces to one.

We present a numerical example comparing the MIMO capacity for different array configurations, approximated as $C \approx \text{EDoF} \log_2(1 + \rho/\text{EDoF}^2)$, where $\rho = \frac{PN_tN_r}{\sigma^2}$, and P is the transmitted power. The receiver employs a URA with fixed $\eta = 256 \times 4$ elements operating at 15 GHz, while the transmitter varies $\eta \in \{512, 256, 128, 1\}$. In all cases, $N_t = N_r = 1024$, and the SNR is set to 20 dB. The resulting capacity, plotted in Fig. 15, shows that the URA with $\eta = 512$ achieves the highest capacity across all distances. This superior performance arises from the enhanced EDoF, which is maximized for elongated URAs compared to square URAs (see Fig. 13). Moreover, for all configurations, the capacity within the r_{rd1} region significantly exceeds that of the far-field rank-one channel. The vertical dashed lines in Fig. 15 indicate the r_{rd1} boundary for each configuration. We employ EDoF₅ to evaluate the capacity, which does not reduce to one at the r_{rd1} (as also observed in Fig. 14), so the capacity at this point remains higher than the far-field value. EDoF₄ is not used because it relies on hard thresholding, which may allocate zero power to channels with singular values below the chosen threshold. While this work primarily focuses on LoS propagation, near-field operation can also yield a higher EDoF in non-line-of-sight (NLoS) scenarios. The EDoF of MIMO channels under NLoS conditions is strongly influenced by the geometric distribution of scatterers. In rich scattering environments, where scatterers span the full angular domain, the MIMO channel can achieve full rank in both near-field and far-field regimes. In contrast, under sparse or limited scattering, the near-field may provide a higher channel rank due to its superior lateral resolution at shorter distances. However, large-scale arrays introduce spatial nonstationarity (SNS), manifested as significant power variations across the antenna elements. SNS primarily arises from partial blockage by finite-sized objects and from incomplete scattering, where objects do not interact uniformly with all antenna elements. The proposed DFT-based method for computing the EDoF is not directly applicable under such conditions. In this case, the visibility regions of the array must first be identified to account for SNS effects, after which the DFT-based approach can be applied within each visible region.

VI. CODEBOOK DESIGN AND CHANNEL ESTIMATION

The insights from Section III on beamdepth and EBRD, combined with the sidelobe suppression explained in Section IV, form the basis for constructing an efficient polar codebook. By leveraging these properties, the proposed codebook is specifically designed to optimize beamforming and compressed sensing (CS)-based channel estimation in the radiative near-field. In this section, we introduce a polar codebook design tailored for a URA, followed by a brief discussion on channel estimation.

The DFT codebook is commonly employed in the far-field to serve as a dictionary for CS-based channel estimation and beam training. It comprises far-field array response vectors $\mathbf{a}_{\text{URA}}(\varphi, \theta)$ obtained by uniform sampling of the directional cosines. In that case, column coherence, which is defined as the maximum of the absolute inner products between two different columns of the dictionary matrix, is zero, since the columns of the DFT

matrix are mutually orthogonal. According to CS theory, a small value of mutual coherence promotes sparsity and thus improves CS-based channel estimation [33].

The near-field codebook Φ , also termed polar codebook, comprises potential near-field array response vectors. The criterion of optimal codebook construction is to minimize the column coherence μ

$$\mu = \max_{p \neq q} \left| \mathbf{b}_{\text{URA}}^H(\varphi_p, \theta_p, r_p) \mathbf{b}_{\text{URA}}(\varphi_q, \theta_q, r_q) \right|^2, \quad (35)$$

where p and q denote the column indices of Φ . The reduction in column coherence μ implies large angle and distance sampling intervals. On the other hand, the sampling intervals should be as small as possible to improve resolution and ensure complete coverage of the near-field region. Therefore, the key design considerations for constructing a polar-domain codebook include reducing column coherence, ensuring complete near-field coverage, and limiting the overall codebook size. Existing methods typically employ uniform sampling in the angle domain and non-uniform sampling in the range domain. In particular, in [6], [18], the maximum admissible range for a given angle pair is determined by a prescribed correlation threshold. However, adopting a lower correlation threshold reduces the maximum allowable sampling distance, which may result in coverage holes in the near-field region. Moreover, this maximum range is agnostic to the EBRD boundary; consequently, complete near-field coverage is not guaranteed.

In contrast, polar codebooks designed based on the beamdepth and the EBRD can effectively reduce the column coherence μ while ensuring uniform 3 dB near-field coverage. In the proposed design, distance sampling starts from a minimum range, and subsequent distance samples are generated until the EBRD limit is reached. Therefore, unlike existing methods, the proposed codebook guarantees complete near-field coverage by construction. The distance-based correlation $\mu_d = \left| \mathbf{b}_{\text{URA}}^H(\varphi_p, \theta_p, r_p) \mathbf{b}_{\text{URA}}(\varphi_p, \theta_p, r_q) \right|$ demonstrates unique characteristics within the radiation field regions defined by the EBRD. In the far-field, $\mu_d \geq 0.5$, making the samples highly correlated in the range dimension. In contrast, μ_d varies with distance relative to the EBRD in the near-field. For near-field array response vectors sampled from outside the EBRD, $\mu_d \geq 0.5$ persists. However, for vectors inside the EBRD and spaced such that the 3 dB points of adjacent beams intersect, $\mu_d \leq 0.1$ is ensured, providing both 3 dB coverage and reduced column coherence. To illustrate, Fig. 16 shows near-field codewords for a ULA at boresight where the adjacent beams intersect at the 0.5 correlation level, ensuring that any LoS user experiences a minimum beamforming gain of 3 dB. Each beam's focal point coincides with a null of the other beams, yielding $\mu_d \approx 0.08$. This value of 0.08 can also be obtained by evaluating the near-field correlation function of a ULA, $\mathcal{G}(\gamma) = \left| \frac{C^2(\gamma) + S^2(\gamma)}{\gamma^2} \right|$, at the first null location. Since $C^2(\gamma) + S^2(\gamma)$ does not reach zero exactly, the first null is approximated by its first minimum, which occurs at $\gamma_{\text{null}} \approx 1.87$, where $\mathcal{G}_{\text{null}} \approx \frac{C^2(1.87) + S^2(1.87)}{1.87^2} \approx 0.08$. The same distance sampling principle is then extended to a URA, as described in Section VI-A2.

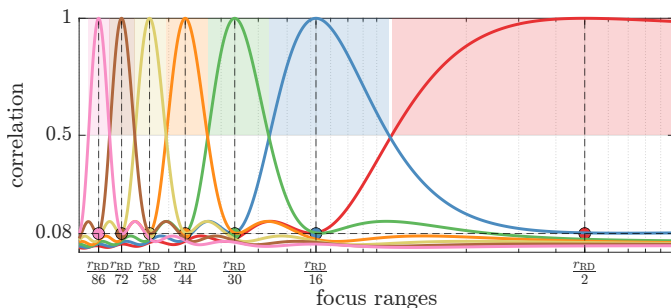


Fig. 16: Correlation between near-field codewords sampled based on proposed distance sampling criteria.

A. Proposed Polar Codebook

Leveraging beamdepth and EBRD expressions derived in Section III, we construct the proposed polar codebook $\Phi \in \mathbb{C}^{N_1 N_2 \times S}$, where S is the total number of polar samples. The proposed scheme relies on sampling a grid of polar points within the EBRD region, followed by generating a near-field codeword for each of the polar points. The algorithmic implementation of the proposed polar codebook is illustrated in Algorithm 1.

1) *Angle Sampling*: For a fixed angle-dependent distance ring, the inner product between two near-field array response vectors $|\mathbf{b}_{\text{URA}}^H(\varphi_p, \theta_p, r_p) \mathbf{b}_{\text{URA}}(\varphi_q, \theta_q, r_q)|$ reduces to sinc functions. To achieve orthogonal codewords, the inner product can be equated to zero, yielding the expressions for azimuth and elevation angles sampling as given in (25a) and (25b), respectively [18]. In line 4 of Algorithm 1, we sample the elevation angle θ_{n_2} , and then use it to sample the azimuth angle φ_{n_1} in line 5.

2) *Distance Sampling*: For a given pair of azimuth and elevation angles, multiple range points are sampled. The range sampling procedure starts with the minimum range set as $2D$ in line 6. Then, in line 7, EBRD is computed as it varies with the azimuth φ and elevation angle θ . EBRD acts as the maximum limit for range sampling. The sampling interval between consecutive distance samples is based on the intersection of the 3 dB points. We sample the range points such that r_F^{\max} in (38a) for the current point coincides with the r_F^{\min} in (38b) for the next point. In line 11, we compute the upper limit of beamdepth \tilde{r}_F^{\max} for the current range sample \tilde{r}_F . Now, we want to find the next point such that its lower limit of beamdepth r_F^{\min} , coincides with \tilde{r}_F^{\max} . To do so, we evaluate (38b) by substituting $r_F^{\min} = \tilde{r}_F^{\max}$ to obtain the focus distance \tilde{r}_F . The steps from lines 10-13 are repeated until the EBRD limit is reached. $S^{(n_1, n_2)}$ denotes the total number of distance samples for a given pair of azimuth φ_{n_1} and elevation angle θ_{n_2} .

3) *Build Dictionary*: For each polar coordinate $(\varphi_{n_1}, \theta_{n_2}, r_s)$, we obtain the near-field array response vector $\mathbf{b}_{\text{URA}} \in \mathbb{C}^{N_{\text{BS}} \times 1}$ in line 17, and apply weight $\mathbf{g}(n)$ as defined in (20), to reduce axial forelobes. The choice of window function $\mathbf{f}(n)$ may vary depending upon the desired sidelobe levels and mainlobe width. Then, the $(N_{\text{BS}} \times S^{(n_1, n_2)})$ sub-matrix $\Phi_{(n_1, n_2)} = [\mathbf{b}_{\text{URA}}(\varphi_{n_1}, \theta_{n_2}, r_1), \dots, \mathbf{b}_{\text{URA}}(\varphi_{n_1}, \theta_{n_2}, r_{S^{(n_1, n_2)}})]$, is constructed by concatenating $S^{(n_1, n_2)}$ near-field array

Algorithm 1: Polar Codebook Design for URA

Input : $\lambda, N_1, N_2, D, r_{\text{RD}}$
Output : Φ

```

1 Procedure Build Polar Codebook
2   for  $n_1 = -\frac{N_1}{2}$  to  $\frac{N_1}{2}$  do
3     for  $n_2 = -\frac{N_2}{2}$  to  $\frac{N_2}{2}$  do
4        $\theta_{n_2} \leftarrow u_z^{(n_2)}$  // Select  $\theta_{n_2}$  according to (25b)
5        $\varphi_{n_1} \leftarrow u_y^{(n_1)}$  // Select  $\varphi_{n_1}$  according to (25a)
6        $\tilde{r}_F \leftarrow 2D$  // Set  $2D$  as minimum range
7        $r_{\text{EBRD}} \leftarrow (\varphi_{n_1}, \theta_{n_2})$  // Compute EBRD from (11)
8        $r_s \leftarrow \{\emptyset\}$ ,  $s \leftarrow 1$ 
9       while  $\tilde{r}_F \leq r_{\text{EBRD}}$  do
10         $r_s \leftarrow \tilde{r}_F$ 
11         $\tilde{r}_F^{\max} \leftarrow r_s$  // Compute upper limit of
           beamdepth  $\tilde{r}_F^{\max}$  for the focus distance  $r_s$ 
           according to (38a)
12         $\tilde{r}_F \leftarrow \tilde{r}_F^{\max}$  // Compute the next distance sample
            $\tilde{r}_F$  by replacing  $r_F^{\min}$  in (38b) with  $\tilde{r}_F^{\max}$ 
13         $s \leftarrow s + 1$ 
14      end
15       $S^{(n_1, n_2)} \leftarrow s$  // Total distance samples for
            $(\varphi_{n_1}, \theta_{n_2})$ 
16      for  $s = 1$  to  $S^{(n_1, n_2)}$  do
17         $\mathbf{b}_{\text{URA}} \leftarrow \mathbf{b}_{\text{URA}}(\varphi_{n_1}, \theta_{n_2}, r_s) \odot \mathbf{g}(n)$  // Generate
            $\mathbf{b}_{\text{URA}}$  from (2) and apply weight  $\mathbf{g}(n)$ 
18         $\Phi_{(n_1, n_2)} = \Phi_{(n_1, n_2)} \cup \mathbf{b}_{\text{URA}}$ 
19      end
20    end
21  end
22   $\Phi = [\Phi_{(1,1)}, \dots, \Phi_{(n_1, n_2)}, \dots, \Phi_{(N_1, N_2)}]^T$ 
23 end

```

response vectors \mathbf{b}_{URA} for $S^{(n_1, n_2)}$ distance samples. The complete polar codebook Φ for S polar samples is obtained by concatenating the sub-matrix $\Phi_{(n_1, n_2)}$ as

$$\Phi = [\Phi_{(1,1)}, \dots, \Phi_{(n_1, n_2)}, \dots, \Phi_{(N_1, N_2)}]^T. \quad (36)$$

B. CS-based Channel Estimation

Channel estimation in UM-MIMO systems, particularly with HBF, poses significant challenges due to the limited number of RF chains. Since terahertz (THz) and millimeter wave (mmWave) MIMO channels exhibit sparsity in the frequency domain [34], [35], CS-based approaches can be employed to estimate near-field channels with reduced pilot overhead [9]. Unlike the far-field, where sparsity exists in the angular domain, the near-field channel demonstrates sparsity in the polar domain, which is also confined to the EBRD region [8]. To leverage this, the near-field channel $\mathbf{h}[k]$ for k^{th} subcarrier can be sparsely represented in the polar domain as $\mathbf{h}[k] = \Phi \mathbf{h}^\rho[k]$, where $\Phi \in \mathbb{C}^{N_{\text{BS}} \times S}$ denotes the near-field codebook, $\mathbf{h}^\rho[k] \in \mathbb{C}^{S \times 1}$ is the sparse near-field channel vector in the polar domain. The near-field channel can then be estimated using a CS-based algorithm such as beam-focused simultaneous orthogonal matching pursuit (BF-SOMP) in [8], where we utilize the polar codebook proposed in Algorithm 1.

C. Performance Evaluation of Proposed Polar Codebook

We conduct Monte Carlo simulations to evaluate the performance of the proposed polar codebook in multiuser channel estimation. The simulation parameters are listed in Table I. A

TABLE I: Simulation Parameters.

Parameter	Value
URA geometry	30×18
Number of BS antennas (N_{BS})	540
Number of RF chains (N_{RF})	4
Carrier frequency (f_c)	15 GHz
Number of subcarriers (K)	64
Bandwidth (B)	100 MHz
Number of users (M_{UE})	4
Number of paths (L)	3
Users distribution in azimuth	$(-\frac{\pi}{6}, \frac{\pi}{6})$
Users distribution in elevation	$(\frac{\pi}{3}, \frac{2\pi}{3})$
Signal-to-noise ratio (SNR)	10 dB
Pilot training length (Q)	64
Number of Monte Carlo trials	1000

downlink orthogonal frequency-division multiplexing (OFDM) system is considered, operating at a carrier frequency 15 GHz with a bandwidth of 100 MHz and 64 subcarriers. The BS simultaneously serves $M_{UE} = 4$ single-antenna UEs using hybrid precoding. The BS is equipped with $N_{BS} = 540$ antenna elements and $N_{RF} = 4$ RF chains. We assume $L = 3$ paths. Channel estimation performance is quantified in terms of the normalized mean squared error (NMSE), defined as $NMSE = \mathbb{E} \left[\frac{\|\mathbf{H} - \hat{\mathbf{H}}\|_2^2}{\|\mathbf{H}\|_2^2} \right]$. The proposed scheme, referred to as BF-SOMP, is compared against state-of-the-art polar codebooks, including P-SOMP [6], EB-SOMP [18], and a conventional far-field DFT codebook.

The NMSE performance against SNR is illustrated in Fig. 17. The UE distance from the BS is uniformly distributed as $\mathcal{U}[2D, r_{EBRD}]$. We assume transmission of orthogonal pilots; therefore, channel estimation for each UE is carried out independently [36]. The codebook size is kept the same across all schemes to ensure a fair comparison. As observed from Fig. 17, BF-SOMP yields 2 dB NMSE improvement at high SNR values compared to the other polar codebooks. The NMSE performance with respect to the number of pilots is shown in Fig. 18. The pilot length is varied from 24 to 120 while the SNR is fixed at 10 dB. The BF-SOMP consistently outperforms the other polar codebooks, whose NMSE saturates with increasing pilot length, whereas the BF-SOMP continues to improve as the number of pilots increases.

D. Computational Complexity and Column Coherence

The storage requirements and computational complexity of the proposed polar codebook and channel estimation algorithm are compared with FF-SOMP, P-SOMP [6], and EB-SOMP [18], as summarized in Table II.

1) *Storage Requirements*: The azimuth and elevation directional cosines are uniformly quantized as $u_y \in [-1, 1]$ and $u_z \in [-1, 1]$ into N_1 and N_2 samples, respectively, yielding a total of $N_{BS} = N_1 N_2$ angular grid points. For a planar array, however, only those samples that lie within the visible region defined by $u_y^2 + u_z^2 \leq 1$ correspond to physically observable directions. Since the visible region is a unit disk of area π embedded within a square of area 4, the effective number of angular samples is approximately $\frac{\pi}{4} N_1 N_2$. The angular sampling strategy is identical for all considered codebooks; hence, differences in storage requirements arise

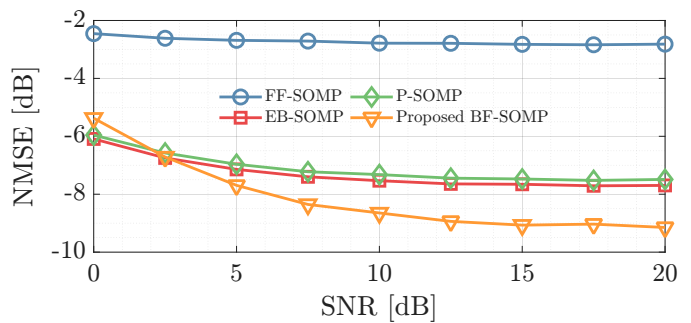


Fig. 17: NMSE performance with respect to SNR.

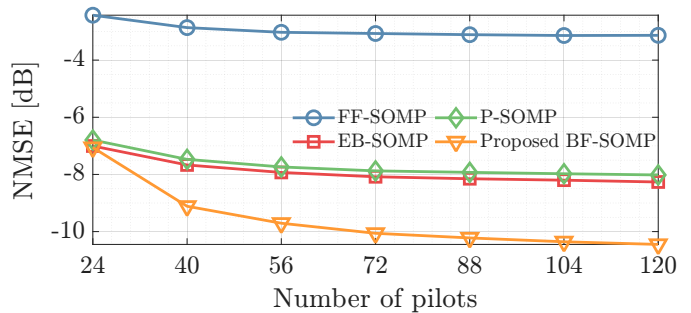


Fig. 18: NMSE performance with respect to pilot length.

solely from their respective range sampling methods. Both the EB-SOMP and P-SOMP codebooks initialize range sampling from a maximum distance Z_Δ , determined by a correlation threshold Δ , and subsequently select distances as Z_Δ/s , where $s = 1, 2, 3, \dots$, until a predefined minimum distance threshold (set to $2D$ here) is reached. For both EB-SOMP and P-SOMP, the maximum sampling distance is chosen close to the EBRD, and the resulting codebook size and coherence are analyzed. By construction, the proposed polar codebook restricts its range sampling exclusively to the EBRD region. Its total size is given by $S_{BF} = \sum_{(n_1, n_2) \in \mathcal{V}} S^{(n_1, n_2)}$, where \mathcal{V} denotes the visible region. For elongated URAs, $S^{(n_1, n_2)} = 6$ for directions close to boresight and gradually decreases to $S^{(n_1, n_2)} = 1$ toward endfire directions. To illustrate the resulting storage requirements, we present a numerical example considering four URA configurations with $N_2 = 64$ fixed and $N_1 \in \{8, 16, 24, 32\}$, corresponding to total antenna counts of $N_{BS} \in \{512, 1024, 1536, 2048\}$. Fig. 19 shows the resulting codebook sizes as a function of the total number of antenna elements. The proposed polar codebook consistently achieves the lowest storage requirement across all configurations. In particular, for $N_{BS} = 2048$, the codebook size of the proposed BF-SOMP scheme is approximately half that of the P-SOMP codebook.

2) *Computational Complexity*: We assume that channel estimation is carried out using the SOMP algorithm. The correlation step primarily dominates its computational complexity and can be expressed as $\mathcal{O}(L Q N_{RF} N_{BS} S_{BF} K)$, where the received pilot matrix of dimension $Q N_{RF} \times K$ is correlated with a codebook of size $N_{BS} \times S_{BF}$ over L propagation paths. Consequently, the differences in computational complexity among the considered schemes arise directly from the size of their respective codebooks, as summarized in Table II.

TABLE II: Codebook size and computational complexity.

Algorithm	Codebook Size	Computational Complexity $\mathcal{O}(\cdot)$
FF-SOMP	$N_{BS} \times N_{BS}$	$\mathcal{O}(LQ N_{RF} N_{BS} K)$
BF-SOMP	$N_{BS} \times S_{BF}$	$\mathcal{O}(LQ N_{RF} S_{BF} K)$
P-SOMP [6]	$N_{BS} \times S_P$	$\mathcal{O}(LQ N_{RF} S_P K)$
EB-SOMP [18]	$N_{BS} \times S_{EB}$	$\mathcal{O}(LQ N_{RF} S_{EB} K)$

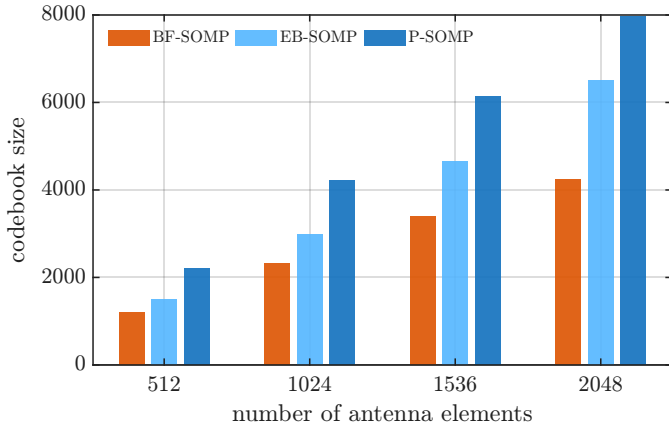


Fig. 19: Codebook size as a function of number of antenna elements.

3) *Column Coherence*: The column coherence defined in (35) is evaluated for all schemes using the same simulation parameters as in the codebook size comparison. The proposed BF-SOMP exhibits a column coherence of approximately 0.26, compared to about 0.45 for P-SOMP and 0.4 for EB-SOMP. For the proposed BF-SOMP, the range samples are selected based on the beamdepth such that their mutual correlation remains below 0.1, as discussed at the beginning of this section. The coherence value of approximately 0.26 originates from the angular domain, since the angular samples are not perfectly orthogonal. Achieving near-zero correlation in the angular domain would require the range samples associated with the same angle to be selected from distinct distance rings, as adopted in [18]. While this approach improves angle domain orthogonality, it introduces stronger correlations among the range samples. In contrast, the proposed method samples the range dimension based on the beamdepth criterion, which simultaneously reduces the overall coherence, ensures complete near-field coverage, and lowers the storage requirements.

VII. CONCLUSION

In this paper, we have derived the angle-dependent beamdepth and the EBRD for a generalized URA. The results show that, for a fixed number of elements, the array geometry has a pronounced impact on the beamdepth, whereas under a fixed aperture constraint, this effect becomes negligible. The near-field beam pattern analysis further reveals that the lateral resolution, determined by the beamwidth, surpasses the axial resolution, governed by the beamdepth. Moreover, amplitude weighting introduces a tradeoff between axial and lateral sidelobe levels. We have also derived an EDoF expression for LoS MIMO systems and compared it across different array geometries, showing that the ULA achieves a higher EDoF than a square URA. Finally, building on the beamdepth and EBRD analysis, we have proposed a polar codebook that enhances

channel estimation performance while reducing computational complexity.

REFERENCES

- [1] A. Hussain, A. Abdallah, A. Celik, and A. M. Eltawil, "Analyzing URA geometry for enhanced spatial multiplexing and extended near-field coverage," in *IEEE PIMRC Conf.*, 2025.
- [2] —, "Near-field ISAC: Synergy of dual-purpose codebooks and space-time adaptive processing," *IEEE Wireless Commun.*, vol. 32, no. 4, pp. 64–70, 2025.
- [3] A. Abdallah, A. Hussain, A. Celik, and A. M. Eltawil, "Exploring frontiers of polar-domain codebooks for near-field channel estimation and beam training: A comprehensive analysis, case studies, and implications for 6G," *IEEE Signal Process. Mag.*, vol. 42, no. 1, pp. 45–59, 2025.
- [4] Qualcomm Technologies, Inc., "GIGA-MIMO is the foundation for wide area 6G," 2024. [Online]. Available: <https://content.rcrwireless.com/giga-mimo>
- [5] P. Ramezani, A. Kosasih, A. Irshad, and E. Björnson, "Exploiting the depth and angular domains for massive near-field spatial multiplexing," *IEEE BITS Inf. Theory Mag.*, vol. 3, no. 1, pp. 14–26, Mar. 2023.
- [6] Z. Wu and L. Dai, "Multiple access for near-field communications: SDMA or LDMA?" *IEEE J. Sel. Areas Commun.*, vol. 41, no. 6, pp. 1918–1935, 2023.
- [7] A. Kosasih, Ö. T. Demir, N. Kolomvakis, and E. Björnson, "Spatial frequencies and degrees of freedom: Their roles in near-field communications," *IEEE Signal Process. Mag.*, vol. 42, no. 1, pp. 33–44, 2025.
- [8] A. Hussain, A. Abdallah, and A. M. Eltawil, "Redefining polar boundaries for near-field channel estimation for ultra-massive MIMO antenna array," *IEEE Trans. Wireless Commun.*, pp. 1–1, 2025.
- [9] M. Cui and L. Dai, "Channel estimation for extremely large-scale MIMO: Far-field or near-field?" *IEEE Trans. on Commun.*, vol. 70, no. 4, pp. 2663–2677, 2022.
- [10] E. Björnson, Ö. T. Demir, and L. Sanguinetti, "A primer on near-field beamforming for arrays and reconfigurable intelligent surfaces," in *Proc. Asilomar Conf. on Signal, Syst., and Comput.*, USA, Mar. 2021, pp. 105–112.
- [11] A. Kosasih and E. Björnson, "Finite beam depth analysis for large arrays," *IEEE Trans. Wireless Commun.*, vol. 23, no. 8, pp. 10 015–10 029, Aug. 2024.
- [12] A. Pizzo, T. L. Marzetta, and L. Sanguinetti, "Degrees of freedom of holographic MIMO channels," in *21st SPAWC*. IEEE, 2020, pp. 1–5.
- [13] S. Hu, F. Rusek, and O. Edfors, "Beyond massive MIMO: The potential of data transmission with large intelligent surfaces," *IEEE Trans. Signal Process.*, vol. 66, no. 10, pp. 2746–2758, 2018.
- [14] A. Hussain, A. Abdallah, and A. M. Eltawil, "Near-field channel estimation for ultra-massive MIMO antenna array with hybrid architecture," in *Proc. IEEE Wireless Commun. and Netw. Conf. (WCNC)*, 2024, pp. 1–6.
- [15] M. Cui and L. Dai, "Near-field wideband beamforming for extremely large antenna arrays," *IEEE Trans. Wireless Commun.*, vol. 23, no. 10, pp. 13 110–13 124, Oct. 2024.
- [16] N. Deshpande, M. R. Castellanos *et al.*, "A wideband generalization of the near-field region for extremely large phased-arrays," *IEEE Wireless Communications Letters*, vol. 12, no. 3, pp. 515–519, Mar. 2022.
- [17] Y. Liu, Z. Wang, J. Xu, C. Ouyang, X. Mu, and R. Schober, "Near-field communications: A tutorial review," *IEEE Open J. Commun. Soc.*, 2023.
- [18] T. Demir and E. Björnson, "A new polar-domain dictionary design for the near-field region of extremely large aperture arrays," in *CAMSAP*, 2023, pp. 251–255.
- [19] J. Sherman, "Properties of focused apertures in the fresnel region," *IEEE Trans. Antennas Propag.*, vol. 10, no. 4, pp. 399–408, Jul. 1962.
- [20] A. Hussain, A. Abdallah, A. Celik, and A. M. Eltawil, "Uniform circular arrays in near-field: Omnidirectional coverage with limited capacity," *arXiv preprint arXiv:2511.12750*, 2025.
- [21] R. C. Hansen, *Phased array antennas*. John Wiley & Sons, 2009.
- [22] E. Björnson and Ö. T. Demir, *Introduction to multiple antenna communications and reconfigurable surfaces*. Now Publishers, Inc., 2024.
- [23] M. A. Richards *et al.*, *Fundamentals of radar signal processing*. McGraw-hill New York, 2005, vol. 1.
- [24] W. Graham, "Analysis and synthesis of axial field patterns of focused apertures," *IEEE Trans. Antennas Propag.*, vol. 31, no. 4, pp. 665–668, 1983.
- [25] R. B. Blackman and J. W. Tukey, "The measurement of power spectra from the point of view of communications engineering—part i," *Bell System Technical Journal*, vol. 37, no. 1, pp. 185–282, 1958.

- [26] A. Hussain, A. Sultan, A. Abdallah, A. Celik, and A. M. Eltawil, "Near field tapering with slepian window: Balancing the range angle sidelobe trade off," *arXiv preprint arXiv:2511.12733*, 2025.
- [27] Y. Lu, Z. Zhang, and L. Dai, "Hierarchical beam training for extremely large-scale MIMO: From far-field to near-field," *IEEE Trans. on Commun.*, vol. 72, no. 4, pp. 2247–2259, 2024.
- [28] C. Ouyang, Y. Liu, X. Zhang, and L. Hanzo, "Near-field communications: A degree-of-freedom perspective," *arXiv preprint arXiv:2308.00362*, 2023.
- [29] D. A. B. Miller, "Communicating with waves between volumes: evaluating orthogonal spatial channels and limits on coupling strengths," *Appl. Opt.*, vol. 39, no. 11, pp. 1681–1699, Apr 2000.
- [30] H. L. Van Trees, *Optimum array processing: Part IV of detection, estimation, and modulation theory*. John Wiley & Sons, 2002.
- [31] S. Sun, R. Li, C. Han, X. Liu, L. Xue, and M. Tao, "How to differentiate between near field and far field: Revisiting the Rayleigh distance," *IEEE Commun. Magz.*, vol. 63, no. 1, pp. 22–28, 2025.
- [32] Y. Lu and L. Dai, "Near-field channel estimation in mixed LoS/NLoS environments for extremely large-scale MIMO systems," *IEEE Trans. on Commun.*, vol. 71, no. 6, pp. 3694–3707, 2023.
- [33] M. A. Davenport, M. F. Duarte, Y. C. Eldar, and G. Kutyniok, "Introduction to compressed sensing," 2012.
- [34] W. Hong, Z. H. Jiang, C. Yu, D. Hou, H. Wang, C. Guo, Y. Hu, L. Kuai, Y. Yu, Z. Jiang *et al.*, "The role of millimeter-wave technologies in 5G/6G wireless communications," *IEEE Journal of Microwaves*, vol. 1, no. 1, pp. 101–122, Jan. 2021.
- [35] Y. Xing, T. S. Rappaport, and A. Ghosh, "Millimeter wave and sub-THz indoor radio propagation channel measurements, models, and comparisons in an office environment," *IEEE Commun. Lett.*, vol. 25, no. 10, pp. 3151–3155, Jun. 2021.
- [36] X. Zhang, H. Zhang, and Y. C. Eldar, "Near-field sparse channel representation and estimation in 6G wireless communications," *IEEE Trans. Commun.*, vol. 72, no. 1, pp. 450–464, Jan. 2024.

APPENDIX A

PROOF OF THEOREM 1

We define $\alpha_{3dB} \triangleq \{(\gamma_1 \gamma_2) \mid \mathcal{G}_{URA}(\gamma_1, \gamma_2) = 0.5\}$. Thus, $\alpha_{3dB} = \frac{N_1 N_2 d^2}{2\lambda} \sqrt{\beta_1 \beta_2} z_{\text{eff}}$. Substituting $d^2 = D^2 / (N_1^2 + N_2^2)$, α_{3dB} can be obtained as

$$\begin{aligned} \alpha_{3dB} &= \frac{r_{RD} N_1 N_2}{4(N_1^2 + N_2^2)} \sqrt{\beta_1 \beta_2} z_{\text{eff}} \\ &= \frac{r_{RD}}{4} \left(\frac{\eta}{\eta^2 + 1} \right) \sqrt{\beta_1 \beta_2} z_{\text{eff}}, \end{aligned} \quad (37)$$

where $\eta = N_1 / N_2$. We can then solve for z in (37) to get $z = \frac{r_F r_{RD} \sqrt{\beta_1 \beta_2} \eta}{r_{RD} \eta \sqrt{\beta_1 \beta_2} \pm 4 r_F \alpha_{3dB} (\eta^2 + 1)}$. Hence,

$$r_F^{\max} = \frac{r_F r_{RD} \sqrt{\beta_1 \beta_2} \eta}{r_{RD} \eta \sqrt{\beta_1 \beta_2} - 4 r_F \alpha_{3dB} (\eta^2 + 1)}, \quad (38a)$$

$$r_F^{\min} = \frac{r_F r_{RD} \sqrt{\beta_1 \beta_2} \eta}{r_{RD} \eta \sqrt{\beta_1 \beta_2} + 4 r_F \alpha_{3dB} (\eta^2 + 1)}. \quad (38b)$$

The distance window between r_F^{\max} and r_F^{\min} is the interval where \mathcal{G}_{URA} is less than or equal to 3 dB. Therefore, $r_{BD} = r_F^{\max} - r_F^{\min}$ is given by (10), which completes the proof.

APPENDIX B

PROOF OF THEOREM 2

In (10), the maximum value of r_{BD} is obtained when the factor in the denominator $[\eta r_{RD} \sin \theta \sqrt{1 - \sin^2 \theta \sin^2 \varphi}]^2 - [4\alpha_{3dB} r_F (\eta^2 + 1)]^2 = 0$. Thus, the farthest angle-dependent axial distance r_F , within which finite-depth beamforming can be achieved, is given by $r_F < \frac{\eta r_{RD}}{4\alpha_{3dB} (1 + \eta^2)} \sin \theta \sqrt{1 - \sin^2 \theta \sin^2 \varphi}$. Otherwise, for distances exceeding this limit, the beamdepth approaches infinity ($r_{BD} \rightarrow \infty$).

APPENDIX C PROOF OF THEOREM 3

The near-field array response vector for the n^{th} antenna element of a ULA is $\mathbf{b}_n(\varphi, r) \approx \frac{1}{\sqrt{N}} e^{-j\nu\{nd \sin(\varphi) - \frac{1}{2r} n^2 d^2 \cos^2(\varphi)\}}$. The tapered axial beam pattern can be obtained by $\mathcal{G}(\varphi, r) = \left| (\mathbf{g} \odot \mathbf{b}(\varphi, r_F))^H \mathbf{b}(\varphi, r) \right|^2$, yielding

$$\mathcal{G}(\varphi, r) = \left| \frac{1}{N_{BS}} \int_{-N_{BS}/2}^{N_{BS}/2} \mathbf{g}(n) e^{-jn^2 \beta_1} dn \right|^2, \quad (39)$$

where $\beta_1 = \nu d^2 \cos^2(\varphi) r_{\text{eff}}$. In the far-field, the lateral pattern of $\mathbf{f}(n)$ is obtained by computing its Fourier transform as

$$\mathcal{G}(\theta) = \left| \int_0^{N_{BS}} \mathbf{f}(n) e^{-jn\beta_2} dn \right|^2, \quad (40)$$

where $\beta_2 = \nu d \sin(\theta)$. The proposed synthesis method reformulates (39) to resemble (40), allowing the desired weighting function $\mathbf{f}(n)$ to be specified and then mapped back to $\mathbf{g}(n)$ that can suppress axial forelobes. Introducing the transformation $t = n^2$, the integral in (39) can equivalently be rewritten as

$$\mathcal{G}(\theta, r) = \left| \frac{1}{N_{BS}} \int_{t \in \mathcal{T}} \frac{\bar{\mathbf{w}}(+\sqrt{t}) + \bar{\mathbf{w}}(-\sqrt{t})}{2\sqrt{t}} e^{-jt\beta_1} dt \right|^2, \quad (41)$$

where $\mathcal{T} = [0, (N_{BS}/2)^2]$. Since (41) has a form similar to (40), the transformation $\mathbf{g}(n) = |n| \mathbf{f}(n^2)$ can be employed to derive the window function to reduce the axial forelobes.

APPENDIX D

PROOF OF THEOREM 4

We rewrite the summation over N_1 in (27) by completing the square as

$$\left| \frac{1}{N_1} \sum_{-\frac{N_1}{2}}^{\frac{N_1}{2}} e^{-j\pi(A_1 n_1 - A_2)} \right|^2 = |F(A_1, A_2)|^2, \quad (42)$$

where $A_1 = \sqrt{\frac{d(1-u_y^2)}{2r_F}}$ and $A_2 = \frac{1}{A_1} \left(\frac{u_y - u_y^{(n_1)}}{2} \right)$. Then, the summation in $F(A_1, A_2)$ can be approximated as

$$\begin{aligned} F(A_1, A_2) &\stackrel{(b_1)}{\approx} \frac{1}{N_1} \int_{-\frac{N_1}{2}}^{\frac{N_1}{2}} e^{-j\pi(A_1 n_1 - A_2)} dn_1 \\ &\stackrel{(b_2)}{=} \frac{1}{\sqrt{2} A_1 N_1} \int_{-\frac{1}{\sqrt{2}} A_1 N_1 - \sqrt{2} A_2}^{\frac{1}{\sqrt{2}} A_1 N_1 - \sqrt{2} A_2} e^{j\pi \frac{t^2}{2}} dt \end{aligned} \quad (43)$$

where (b₁) is accurate when $N_1 \rightarrow \infty$, and (b₂) is obtained by letting $A_1 n_1 - A_2 = \frac{1}{\sqrt{2}} t$. Next, based on the Fresnel integrals, we have $F(A_1, A_2)$ as

$$\begin{aligned} &= \frac{\int_0^{\frac{1}{\sqrt{2}} A_1 N_1 - \sqrt{2} A_2} e^{j\pi \frac{t^2}{2}} dt - \int_0^{-\frac{1}{\sqrt{2}} A_1 N_1 - \sqrt{2} A_2} e^{-j\pi \frac{t^2}{2}} dt}{\sqrt{2} A_1 N_1} \\ &= \frac{C(\gamma_1 + \gamma_2) - C(\gamma_1 - \gamma_2) + j(S(\gamma_1 + \gamma_2) - S(\gamma_1 - \gamma_2))}{2\gamma_2} \end{aligned} \quad (44)$$

where $\gamma_1 = (u_y^{(n_1)} - u_y) \sqrt{\frac{r_F}{d(1-u_y^2)}}$, $\gamma_2 = \frac{N_1}{2} \sqrt{\frac{d(1-u_y^2)}{r_F}}$.
 The factor involving summation over N_2 can be evaluated analogously, thereby completing the proof.